Earth-Science Reviews 196 (2019) 102874

Contents lists available at ScienceDirect

Earth-Science Reviews

journal homepage: www.elsevier.com/locate/earscirev

Variability of subducting slab morphologies in the mantle transition zone: Insight from petrological-thermomechanical modeling

Zhong-Hai Li[a,b,*], Taras Gerya[c], James A.D. Connolly[c]

[a] Key Laboratory of Computational Geodynamics, College of Earth and Planetary Sciences, University of Chinese Academy of Sciences, Beijing, China
[b] Laboratory for Marine Geology, Qingdao National Laboratory for Marine Science and Technology, Qingdao, China
[c] Department of Earth Sciences, ETH-Zurich, Switzerland

ARTICLE INFO

Keywords:
Subduction mode selection
Mantle transition zone
Phase transition
Aqueous fluid activity
Numerical modeling

ABSTRACT

Variable morphologies of subducting slabs are observed in tomographic images of the mantle transition zone (MTZ), where slabs appear to stagnate in the MTZ or enter the lower mantle. These contrasting morphologies of subducting slabs are dependent on the joint effects of various dynamic, kinematic and geometric factors. Force balance analysis indicates that the favorable conditions of slab stagnation in the MTZ include old/cold slab subducting into the mantle with large Clapeyron slopes at 410 km and 660 km discontinuities, as well as the significant trench retreat and shallow dip angle. However, these conditions are often not achieved together for specific subduction zones on the Earth, which thus require systematic studies to distinguish their relative effects. Here, we analyze the slab mode selection in the MTZ based on coupled petrological-thermomechanical numerical model. The model results indicate that (1) water activity and partial melting weaken the subduction channel and form a hot and weak mantle wedge beneath the island arc that affects slab dynamics. (2) The Clapeyron slope of phase transition at 660 km can significantly contribute to the slab stagnation in the MTZ, whereas the Clapeyron slope at 410 km does not change the general mode selection, but does affect the trench motion and further the length of flattened slab. (3) A sharp viscosity jump between the lower and upper mantles can promote slab stagnation in the MTZ, which has a similar effect with a strong viscosity-depth gradient. (4) Fast trench retreat is the most critical factor controlling slab stagnation, especially the long slab flattening in the MTZ. (5) The age/thickness of converging plates can also influence the slab/MTZ interaction by modifying the slab dip angle and trench motion. (6) A thin, weak layer at the bottom of MTZ does not play significant roles in the slab mode selection. The combined force balance analysis and numerical studies are compared with the comprehensive observations of natural subduction zones, which improve understanding of the dynamics of slab/MTZ interaction and the resulting variability of subducting slab morphologies.

1. Introduction

The mantle transition zone (MTZ) between the 410 km and 660 km discontinuities is a special and important layer, which has multiple phase transitions and probably larger water capacity than both the upper and lower mantles, although whether it actually does contain a lot of water is far from certain (e.g., Bina and Helffrich, 1994; Karato, 2011). Thereby, it may play significant roles in affecting the styles and dynamics of subducting slabs. Global seismic tomography reveals variable morphologies of sinking slabs in the MTZ (Fig. 1). In some regions, the slabs sink through the MTZ and directly into the lower mantle, such as Cocos and Peru (slab of green colour in Fig. 1) (e.g., Grand et al., 1997; Goes et al., 2008), whereas some subducting slabs appear to stagnate and flatten in the MTZ, e.g., Japan, Aleutian, Tonga (slab of blue colour in Fig. 1) (e.g., van der Hilst, 1995; Huang and Zhao, 2006; Fukao and Obayashi, 2013). In some other subduction zones, the slab styles in the MTZ are not quite clear, which might either indicate the transition between contrasting modes, or be the result of limited resolution of seismic tomography (slab of grey colour in Fig. 1).

A number of possible mechanisms have been proposed for explaining the variable modes of slab and MTZ interaction (e.g., Goes et al., 2017), which can be summarized into the following three groups:

(i) Dynamic factors (viscosity, density, slab age)

The average viscosity of the lower mantle is generally constrained to

* Corresponding author at: Key Laboratory of Computational Geodynamics, College of Earth and Planetary Sciences, University of Chinese Academy of Sciences, Beijing, China.
E-mail address: li.zhonghai@ucas.ac.cn (Z.-H. Li).

https://doi.org/10.1016/j.earscirev.2019.05.018
Received 16 March 2019; Received in revised form 30 May 2019; Accepted 30 May 2019
Available online 03 June 2019
0012-8252/

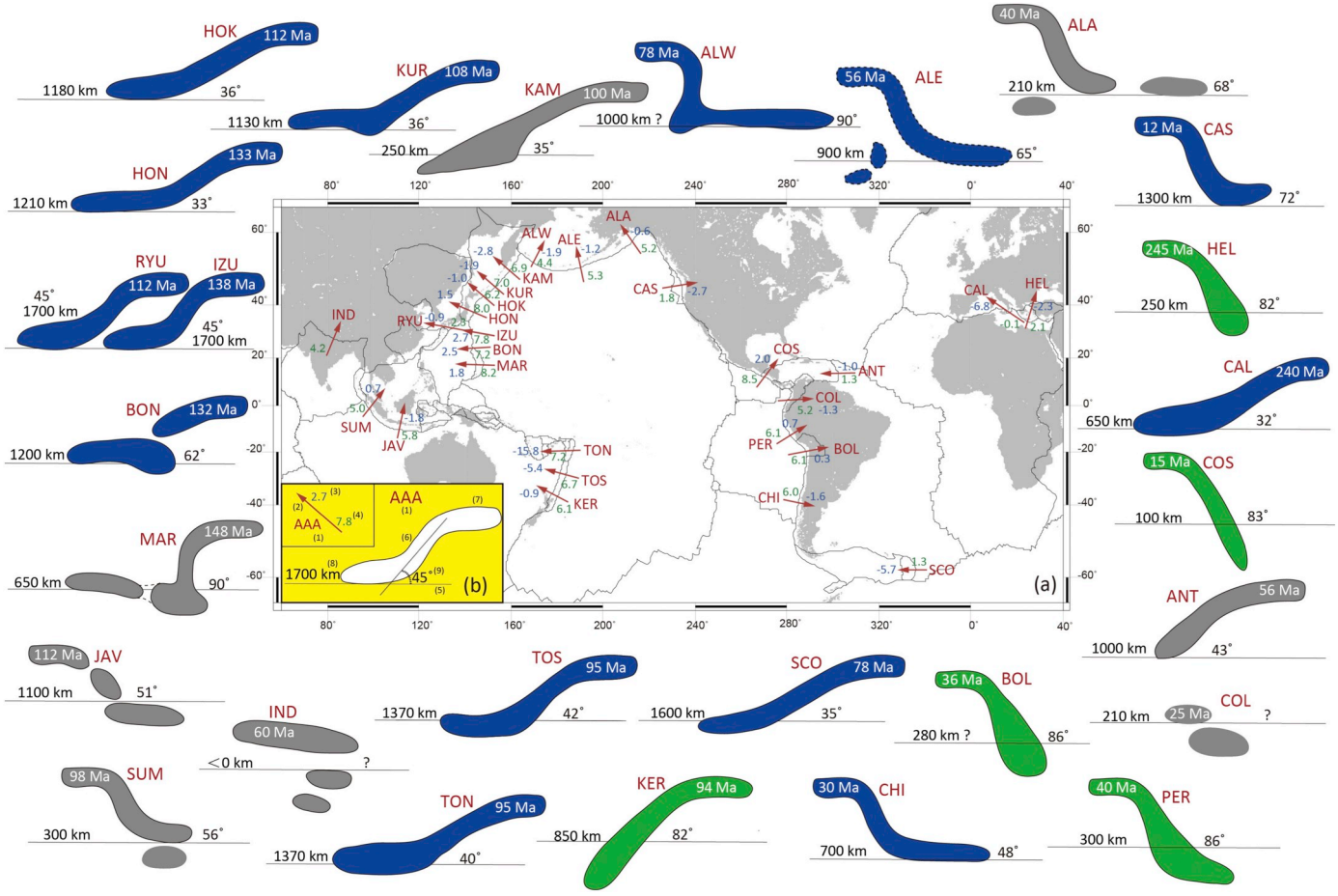

Fig. 1. Compilation of slab morphologies in the mantle transition zone (MTZ) with the relevant parameters of slab dip angle in the upper mantle, slab age at the trench, trench retreat length in the past ~50 Ma, as well as the present-day velocities of subducting plate movement and trench migration. The colors of slab contours indicate subduction modes in the MTZ: blue for slab stagnation, green for slab penetration, and grey for the slab styles not quite clear. (a) The position of selected profiles in the global subduction system, referring to Schellart et al. (2011) and Goes et al. (2017). (b) For a specific subduction zone, several definitions/parameters are illustrated: (1) The name abbreviation of subduction zone as shown below in (c); (2) Red arrow for the position and direction of subduction; (3–4) Blue number for the trench velocity in cm/yr with negative value for retreating, whereas green number for the velocity in cm/yr of the subducting plate. These values are from Schellart et al. (2011), which were calculated in the Indo-Atlantic hot spot reference frame from O'Neill et al. (2005) using the geophysical relative plate motion model from DeMets et al. (1994) for motion of the major plates and using numerous microplate motions and backarc/arc/fore-arc deformation rates from the sources as summarized by Schellart et al. (2008) and Schellart (2008). (5) Thin black line for the 660 km discontinuity; (6) The contour for the slab morphology following the seismic tomographic dataset of GAP-P4 (*www.csmap.jamstec.go.jp*; based on Fukao and Obayashi, 2013; Obayashi et al., 2013); (7) White number in Ma for the age of subducting plate at the trench (*www.ngdc.noaa.gov*); (8) Black number in km for the estimated length of trench retreat during the past ~50 Ma (Goes et al., 2017; with necessary interpolations); (9) Black number in ° for the approximated dip angle of the slab morphology in the upper mantle. (c) Names and abbreviations of the selected subduction zones: JAV-Java; SUM-Sumatra; IND-India; KER-Kermadec; TON-Tonga; TOS-Southern Tonga; MAR-Marianas; BON-Bonin; IZU-Izu; RYU-Ryukyu; HON-Honshu; HOK-Hokkaido; KUR-Kuriles; KAM-Kamchatka; ALW-Western Aleutians; ALE-Aleutians; ALA-Alaska; CAS-Cascadia; COS-Cocos; ANT-Antilles; COL-Colombia; PER-Peru; BOL-Bolivia; CHI-Chile; SCO-Scotia; CAL-Calabria; HEL-Hellenic. (For interpretation of the references to colour in this figure legend, the reader is referred to the web version of this article.)

be 10–100 higher than the average upper mantle viscosity, according to the combined geoid, postglacial rebound, gravity and dynamic topography, etc. (Hager, 1984; Mitrovica and Forte, 2004; Steinberger and Calderwood, 2006; Forte et al., 2010; Čížková et al., 2012). Numerical models get a range of slab morphologies with such a viscosity ratio between the lower and upper mantles (e.g., Gurnis and Hager, 1988; Christensen, 1996; Garel et al., 2014; Agrusta et al., 2017), which are thus consistent with the diversity of slab styles according to the tomographic observations (Fig. 1). However, the long (> 1000 km) stagnant slab (e.g., beneath Japan and eastern Asia) is not predicted in the models with only such a viscosity jump/increase (Garel et al., 2014). Alternatively, if there is no viscosity jump, it is hard to develop flat slab stagnation (Yanagisawa et al., 2010; Agrusta et al., 2017). It indicates that the viscosity increase between the lower and upper mantles is necessary but not sufficient condition for the observed slab stagnations in nature. It is worth noting that a strong viscosity-depth gradient may have a similar dynamic effect as a sharp viscosity jump between the lower and upper mantles (Goes et al., 2017).

The endothermic phase transition (ringwoodite − > bridgmanite + magnesiowüstite) at 660 km discontinuity has a negative Clapeyron slope (Table 1) (e.g., Bina and Helffrich, 1994). It can result in a local increase of buoyancy in the subducting slab when entering the lower mantle, which thus provides a main resistance and contributes to slab stagnation (Ringwood, 1975; Ito and Yamada, 1982). Many modeling studies have been conducted to investigate how the slab interacted with the 660 km discontinuity (e.g., Christensen and Yuen, 1984; Tackley et al., 1993; Agrusta et al., 2017). It generally indicates that the higher Clapeyron slope will lead to slab stagnation in the MTZ, whereas lower slope has little effects. In contrast to the endothermic phase transition at 660 km, the exothermic phase transition (olivine − > wadsleyite) and

Table 1
Summary of measured Clapeyron (pressure/temperature) slopes of 660 km phase transition.

$-C_{660}$ (MPa/K)[a]	References
2	Ito and Yamada, 1982
2.8	Ito and Takahashi, 1989
4 ± 2	Ito et al., 1990
3 ± 1	Akaogi and Ito, 1993
2.5 ± 0.4	Chopelas et al., 1994
1.9–2.1	Bina and Helffrich, 1994
2.8	Hirose, 2002
0.4–2	Katsura et al., 2003
1.3	Fei et al., 2004
2 (hydrous)	Litasov et al., 2005a
0.5 (dry)	Litasov et al., 2005b
2.6 ± 0.2	Akaogi et al., 2007

[a] Note that the values of C_{660} are negative.

Table 2
Summary of measured Clapeyron (pressure/temperature) slopes of 410 km phase transition.

C_{410} (MPa/K)	References
3.5	Suito, 1977
2.5	Ashida et al., 1987
2.5	Katsura and Ito, 1989
1.5 ± 0.5	Akaogi et al., 1989
2.7	Chopelas, 1991
2.9–3.0	Bina and Helffrich, 1994
3.6 ± 0.2	Morishima et al., 1994
3.1 ± 0.2	Akaogi et al., 2007

its positive Clapeyron slope at 410 km (Table 2) (e.g., Bina and Helffrich, 1994) can lead to local density increase and thus enhance the slab sinking in the transition zone (Christensen, 1996; Čížková et al., 2002). However, it has been further proposed that this phase transition could be kinetically delayed in the cold cores of sinking slabs, forming the metastable olivine (Rubie and Ross, 1994; Bina et al., 2001; Mosenfelder et al., 2001; Tetzlaff and Schmeling, 2009) or metastable pyroxene (Hogrefe et al., 1994; Nishi et al., 2008; van Mierlo et al., 2013). In such cases, the opposite effect would be reducing the negative buoyancy of cold slabs and resisting the slab sinking. It will thus contribute to the slab stagnation in the MTZ, which has been systematically studied by the numerical models (Agrusta et al., 2014; King et al., 2015). Besides the above main phase transitions, there are several others, e.g., the phase transition at 520 km from wadsleyite to ringwoodite (Katsura and Ito, 1989), the transition from garnet to bridgmanite at 660 km with a probably positive Clapeyron slope (Hirose, 2002; Stixrude and Lithgow-Bertelloni, 2011; Holland et al., 2013). The dynamic effects of the interplay of these transitions remain uncertain.

The thermal structure of subducting slab is strongly dependent on the slab age, which will further affect the rheological properties, as well as the phase transitions and density variations. Thus the age of subducting slab may play significant roles in the mode selection of slab/MTZ interaction. Indeed, the stagnant slabs are more common in the western Pacific (Fig. 1), where older lithospheres of 90–150 Ma are subducting (Müller et al., 2008). Alternatively, some deeply penetrating slabs are observed in the eastern Pacific (Fig. 1), with relatively younger lithospheres of 0–50 Ma (Müller et al., 2008). However, there are further complexities with many subducting slabs inconsistent with the above rules, e.g., the Cascadia and Mariana (Fig. 1). In addition, it has generally been observed that there is no simple correlation between the present-day slab dip angle and its age at the trench (Lallemand et al., 2005; Sdrolias and Müller, 2006). It indicates that the subduction mode selection in the MTZ cannot be solely explained by the slab age.

(ii) Kinematic factors (plate and trench motions)

Generally, the rates of downgoing plate motions range from several cm/yr up to 10 cm/yr (Müller et al., 2008; Goes et al., 2011; Zahirovic et al., 2015). A few exceptions exist with notably faster motions of > 10 cm/yr or even > 15 cm/yr, e.g., segments of the Farallon plate as well as the Indian plate before collision with Asia, which require additional forces/mechanisms. For the trench motions, most of them (70%) retreat in Cenozoic, accompanied by fewer stable or advancing ones (Müller et al., 2008; Schellart, 2008; Williams et al., 2015). The rates of trench motions are generally between 1 cm/yr (advancing) and − 2 cm/yr (retreating), with some exceptions of significantly faster retreat during (part of) the Cenozoic, e.g., Tonga, Izu-Bonin and Japan (Williams et al., 2015). Based on the summary of plate age, plate and trench motions as well as the slab morphology for a number of subduction zones (Sdrolias and Müller, 2006), some correlations between the downgoing plate motion and the slab age are indicated; however, there is no correlation between the present-day trench motion and slab morphology in the MTZ (King, 2001; Lallemand et al., 2005; Billen, 2008). Goes et al. (2017) compared the estimated lengths of flattened slabs in the MTZ with the total trench retreat over the past ~50 Ma, which reveals good correlations between them as firstly proposed by Van der Hilst and Seno (1993). The flattened slabs in the MTZ generally have a history of significant trench retreat, whereas slabs penetrating into the lower mantle are consistent with limited trench retreat (Fig. 1). A few exceptions do exist, e.g., Antilles and Kermadec, which indicate the trench motion is not the only control.

(iii) Geometric factors (slab dip angle in the MTZ)

The above-mentioned dynamic and kinematic factors may lead to variable dip angles of subducting slabs in the upper mantle, which would further significantly affect the force balance and finally contribute to the different slab morphologies in the MTZ. Previous numerical models indicate that the slab dip angle when reaching the 660 km discontinuity can strongly modify the subduction mode in the MTZ. Slab flattening is generally predicted in the models with smaller dip angle, whereas slab folding or penetration is easily resulted when the sinking slab is sub-vertical (Li and Ribe, 2012; Shi et al., 2018). In addition, the backward turning of slab with trench advance may be achieved with large dip angles, e.g., > 130° (e.g., Bellahsen et al., 2005; Di Giuseppe et al., 2008; Funiciello et al., 2008; Li and Ribe, 2012).

Based on the summary of dynamic, kinematic and geometric factors, it demonstrates that the old/cold lithosphere with significant trench retreat and shallow dip angle may strongly contribute to the slab flattening in the MTZ. Generally, the style of subduction results from the competition between the time required to bend the plate at the trench and the time available to achieve this bending (Goes et al., 2017). The former is controlled by the resistance for plate bending, while the latter one controlled by the slab pull (density) and the resulted sinking rate. Older slabs with higher strength and higher density require longer time for bending, but shorter time for sinking. Hence, old slabs will normally lead to shallower dips and faster trench retreat, which are all the favorable conditions for slab flattening in the MTZ. However, these dynamic, kinematic and geometric conditions are often not achieved together for specific subduction zones as summarized in Fig. 1, e.g., Mariana. Besides the age of subducting plate, many other factors may also contribute to change the kinematic trench motions and geometric slab dips, e.g., tractions or resistances from the overriding plate and surrounding mantle (e.g., Capitanio et al., 2007, 2010; Rodríguez-González et al., 2012; Čížková and Bina, 2013; Holt et al., 2015; Huangfu et al., 2016). Consequently, the resulting subduction mode in the MTZ could be complex on the Earth, which may be consistent with some of the favorable conditions as discussed above, but conflicted with others (Fig. 1).

In order to better understand the dynamics of subducting slab-MTZ

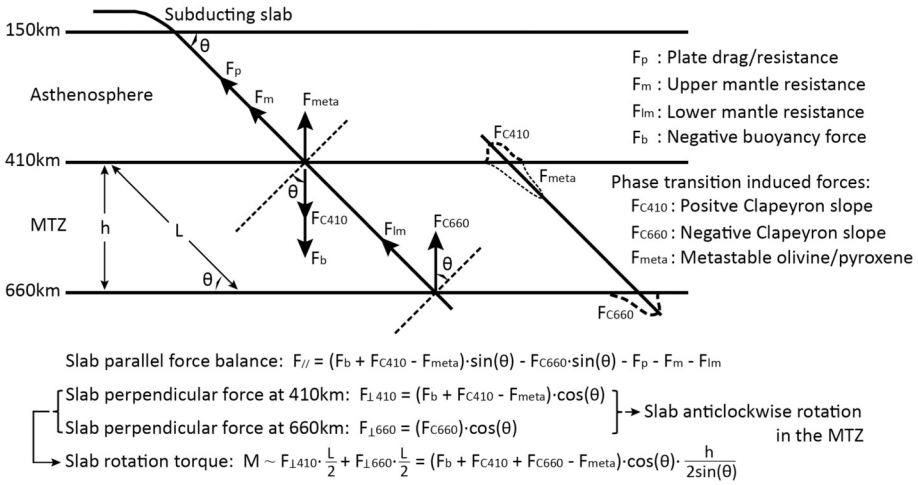

Fig. 2. Force balance analysis of subducting slab in the upper mantle.

interaction, as well as the resulting slab styles, we conducted force balance analysis of the subducting slab in the MTZ, which provides general predictions for the forward numerical modeling. Subsequently, we conducted thermomechanical modeling with integrated visco-plastic-Peierls rheology and thermodynamic fluid-melt activity, which simulates both large-scale geophysical observations and geological/petrological processes during subduction. Based on the numerical models, the effects of possible dynamic, kinematic and geometric factors that may influence the slab mode selection in the MTZ are systematically investigated and compared with the natural observations.

2. Force balance analysis of the slab/MTZ interaction

Many forces act on a subducting slab in the upper mantle (Fig. 2). The overall effects of these forces control the kinematics and dynamics of subduction as well as the mode selection during slab and MTZ interaction. We consider a subducting slab in the sub-lithospheric mantle, i.e. the asthenosphere and MTZ, which indicates that the 410 km discontinuity is approximately located in the middle depth of the region. The forces on the slab at 410 km are summarized in Fig. 2, including a negative buoyancy force (F_b), resistances from the plate (F_p) and the mantle (F_m), as well as the phase transition induced forces, e.g., F_{C410} from the positive Clapeyron slope and F_{meta} from the metastable olivine and pyroxene around 410 km. It is worth noting that the driving (F_b) and resistance (F_p, F_m) forces are not exactly acting on the middle of the slab, but distributed along the slab, which are equivalent only when the slab is rigid. Thus, it is an approximation used for first-order analysis. At the depth of 660 km, two additional forces act on the slab. One is the resistance from the lower mantle due to viscosity jump/increase, the other is from the negative Clapeyron slope of phase transition.

The aforementioned forces can be decomposed into the directions parallel and perpendicular to the slab. The slab parallel forces do not contribute much to the slab rotation required for slab stagnation in the MTZ. In contrast, the slab perpendicular forces at 410 km and 660 km depths act in opposite directions, and contribute to the anticlockwise rotation of the slab, with the resulted rotation torque shown at the bottom of Fig. 2. It indicates that the positive and negative Clapeyron slopes at 410 km and 660 km, respectively, promote the slab rotation and stagnation in the MTZ, which are thus important factors for further study.

The effects of negative slab buoyancy on the mode selection of slab/MTZ interaction are complex. It can contribute to slab rotation and further stagnation by the slab perpendicular force; however, it is also the main force driving slab penetration into the lower mantle in the slab parallel direction. Thus, the effect of negative buoyancy on slab stagnation/penetration is not straightforward. The force induced by the metastable olivine/pyroxene at 410 km will counteract (parts of) the effects of positive Clapeyron slope (F_{C410}), which thus hamper the slab rotation. On the other hand, it will also hamper the slab penetration to the lower mantle, because of the lower density of sinking slab resulted from the delayed phase transition of metastable olivine/pyroxene. These complex effects are partially included in the current numerical models.

According to the analysis of slab rotation torque (Fig. 2), one of the most important factors for slab stagnation is the dip angle (θ). The low slab dip angle can strongly promote the slab rotation and further stagnation in the MTZ, which thus agrees with the predictions as summarized in the Introduction (e.g., Li and Ribe, 2012; Shi et al., 2018). In addition, the trench retreat tends to decrease the slab dip angle if all the other parameters are identical, which could also contribute to slab stagnation (e.g., Goes et al., 2017).

As a summary, the forces induced by the phase transitions at 410 km and 660 km may affect the slab and MTZ interaction. The opposite directions of these forces contribute to slab rotation and further flattening in the MTZ. The slab mode selection in the MTZ is also controlled by the slab dip angle and trench motions, which may be further determined by the properties of the subducting and overriding plates, as well as the kinematic boundary conditions. The analytical studies help to inspire the possible parameters affecting slab/MTZ interaction, e.g., the phase transitions at 410 km and 660 km, which could thus provide general directions for the following thermomechanical modeling studies.

3. Numerical modeling method

The numerical models are conducted with the finite difference code I2VIS, which combines movable Lagrangian markers and fixed Eulerian nodal points (e.g., Gerya, 2010). In this 2-D computing framework, the extended Boussinesq approximations are applied with a rheology considering different non-linear mechanisms and phase transitions in the numerical models.

3.1. Governing equations

Three sets of conservation equations (mass, momentum and energy) as well as the constitutive relationships are solved in the 2-D numerical models.

3.1.1. Stokes equations

$$\frac{\partial \sigma'_{ij}}{\partial x_j} = \frac{\partial P}{\partial x_i} - g_i \rho(C, M, P, T)(i, j = 1, 2) \quad (1)$$

Table 3
Viscous flow laws used in the numerical experiments.[a]

Symbol	Flow law	E (kJ·mol^{-1})	V (J·MPa^{-1}·mol^{-1})	n	A_R (MPa^{-n}·s^{-1})	m	A_K (s^{-1})
A*	Wet quartzite	154	8	2.3	3.2×10^{-4}	–	–
B*	Plagioclase An_{75}	238	8	3.2	3.3×10^{-4}	–	–
C*	Dislocation creep of dry olivine	540	13	3.5	–	0.0	3.5×10^{22}
D*	Diffusion creep of dry olivine	300	4	1.0	–	2.5	8.7×10^{15}
E*	Dislocation creep of wet olivine	430	10	3.0	–	0.0	2.0×10^{18}
F*	Diffusion creep of wet olivine	240	4	1.0	–	2.5	5.3×10^{15}

[a] Viscous parameters of crustal rocks (A* and B*) are from Kirby and Kronenberg (1987) and Ranalli (1995). Viscous parameters of mantle rocks (C*, D*, E*, F*) are from Karato and Wu (1993).

where σ' denotes the deviatoric stress tensor; x represents the spatial coordinate; g is the gravitational acceleration; the density ρ depends on composition (C), melt fraction (M), dynamic pressure (P) and temperature (T). For a specific rock type:

$$\rho = \rho_{\text{solid}} - M(\rho_{\text{solid}} - \rho_{\text{molten}})$$
$$\rho_{\text{solid | molten}} = \rho_0[1 - \alpha(T - T_0)][1 + \beta(P - P_0)] \quad (2)$$

where the densities of solid (ρ_{solid}) and molten rocks (ρ_{molten}) are further calculated depending on the specific pressure and temperature, in which ρ_0 is the density under the reference condition with $P_0 = 0.1$ MPa and $T_0 = 298$ K. α and β are the thermal expansion coefficient and the compressibility coefficient, respectively (Table 4). Rock density is further corrected for phase transitions that are explained in Section 4.2.

Further on, the constitutive relationship is shown below:

$$\sigma'_{ij} = 2\eta_{\text{eff}}\dot{\varepsilon}_{ij}$$
$$\dot{\varepsilon}_{ij} = \frac{1}{2}\left(\frac{\partial v_i}{\partial x_j} + \frac{\partial v_j}{\partial x_i}\right) \quad (3)$$

where $\dot{\varepsilon}$ and v are the deviatoric strain rate tensor and velocity vector, respectively. η_{eff} is the effective viscosity, with rheological flow laws illustrated in Section 3.2.

3.1.2. Incompressible continuity equation

The multiple phase transitions and related density changes would challenge the incompressibility. However, for simplicity, the conservation of mass in this study is still approximated by the incompressible continuity equation (extended Boussinesq approximation) (Christensen and Yuen, 1985; Gerya, 2010):

$$\frac{\partial v_i}{\partial x_i} = 0 \quad (4)$$

3.1.3. Energy equation

$$\rho C_p\left(\frac{DT}{Dt}\right) = -\frac{\partial q_i}{\partial x_i} + H$$
$$q_i = -k(C, P, T)\frac{\partial T}{\partial x_i} \quad (5)$$

where C_p is the effective isobaric heat capacity; DT/Dt is the substantive time derivative of temperature; q is the thermal heat flux; k is the thermal conductivity, dependent on composition (C), pressure (P) and temperature (T). H denotes the heat generations, including radioactive heat production (H_r), adiabatic heating (H_a) and shear heating (H_S). H_r depends on the rock composition and is assumed to be constant: H_r = constant(C). H_a is related to pressure changes (compression/decompression): $H_a = T\alpha v_i dP/dx_i$. H_S is related to dissipation of mechanical energy during deformation and depends on the deviatoric stress and deviatoric strain rate: $H_S = \sigma'_{ij}\dot{\varepsilon}_{ij}$.

The effect of latent heating is only applied for the equilibrium crystallization/partial melting; however, it is not used for the other phase transitions, e.g., 410 km or 660 km discontinuities, which may affect the model results in a certain degree as investigated for the mantle convection (Steinberger, 2007). The effect of latent heating due to equilibrium crystallization of molten rocks is included implicitly in the heat conservation equation by increasing the effective heat capacity (Cp_{eff}) and the thermal expansion coefficient (α_{eff}) of the partially crystallized/molten rocks ($0 < M < 1$) as discussed in Gerya (2010), calculated as: $Cp_{\text{eff}} = Cp + Q_L\left(\frac{\partial M}{\partial T}\right)_{P=\text{cnst}}$ and $\alpha_{\text{eff}} = \alpha + \rho\frac{Q_L}{T}\left(\frac{\partial M}{\partial P}\right)_{T=\text{cnst}}$, where M is the volumetric degree of melting, Q_L is the latent heat (Table 4) (Bittner and Schmeling, 1995; Turcotte and Schubert, 2002).

3.2. Visco-Plastic-Peierls rheology

The constitutive relationships between the deviatoric stress and strain rate tensors are described by the combined visco-plastic-Peierls flow laws. For a specific rock type under certain external conditions (e.g., pressure, temperature), the ductile viscosity (η_{ductile}), the plastic equivalent (η_{plastic}), as well as the Peierls viscosity (η_{peierls}) will be calculated separately, based on the experimentally determined flow laws as followed:

3.2.1. Viscous rheology

For the viscous rheology of rocks, we apply different flow laws for the crustal (Ranalli, 1995) and mantle rocks (Karato and Wu, 1993).

(1) Viscous flow law of crustal rocks

The viscosities of both the continental and oceanic crustal rocks are defined according to the flow laws of Ranalli (1995):

$$\eta_{\text{ductile}} = \frac{1}{2}(A_R)^{-\frac{1}{n}}(\dot{\varepsilon}_{II})^{\frac{1-n}{n}}\exp\left(\frac{E + PV}{nRT}\right) \quad (6)$$

where $\dot{\varepsilon}_{II} = (0.5\dot{\varepsilon}_{ij}\dot{\varepsilon}_{ij})^{1/2}$ is the second invariant of the strain rate tensor; A_R (pre-exponential factor), E (activation energy), V (activation volume) and n (creep exponent) are experimentally determined flow law parameters (A* and B* in Table 3) (Kirby and Kronenberg, 1987; Ranalli, 1995); R is the gas constant.

(2) Viscous flow law of mantle rocks

The viscosity of mantle rocks is defined according to Karato and Wu (1993), which integrates both diffusion and dislocation creep:

$$\eta_{\text{diffusion | dislocation}} = \frac{1}{2}(A_K)^{-\frac{1}{n}}u\left(\frac{d}{b}\right)^{\frac{m}{n}}(\dot{\varepsilon}_{II})^{\frac{1-n}{n}}\exp\left(\frac{E + PV}{nRT}\right)$$
$$\frac{1}{\eta_{\text{ductile}}} = \frac{1}{\eta_{\text{diffusion}}} + \frac{1}{\eta_{\text{dislocation}}} \quad (7)$$

where u is the shear modulus (u = 80GPa); d is grain size (d = 1 mm); b is the length of Burgers vector (b = 0.5 nm); m is the grain size exponent. Similarly, A_K (pre-exponential factor), E (activation energy), V (activation volume) and n (creep exponent) are flow law parameters

Table 4
Material properties used in the numerical experiments.[a]

Material (state)	Number in Fig. 4c	ρ_0 (kg·m^{-3})	C_p (J·kg^{-1}·K^{-1})	k (W·m^{-1}·K^{-1})[b]	$T_{solidus}$ (K)[c]	$T_{liquidus}$ (K)[d]	Q_L (kJ·kg^{-1})	H_r (μW·m^{-3})	Viscous Flow law[e]	Plastic C_0 (MPa)[f]	Plastic sin(φ_{eff})[f]
Sticky air	1	1	3.3×10^6	200	–	–	–	0	10^{18} Pa·s	–	–
Sticky water	2	1000	3.3×10^3	200	–	–	–	0	10^{18} Pa·s	–	–
Sediment (solid)	3,4	2600	1000	K_1	T_{S1}	T_{L1}	300	2.0	A*	10–1	0.1–0.05
Sediment (molten)	5	2400	1000	K_1	T_{S1}	T_{L1}	300	2.0	A*	10–1	0
Continental upper crust (solid)	6	2800	1000	K_1	T_{S1}	T_{L1}	300	1.0	A*	10–1	0.1–0.05
Continental upper crust (molten)	7	2400	1000	K_1	T_{S1}	T_{L1}	300	1.0	A*	10–1	0
Continental lower crust (solid)	8	3000	1000	K_1	T_{S3}	T_{L3}	380	1.0	B*	10–1	0.1–0.05
Continental lower crust (molten)	9	2400	1000	K_1	T_{S3}	T_{L3}	380	1.0	B*	10–1	0
Oceanic upper crust (solid)	10	3000	1000	K_2	T_{S2}	T_{L2}	380	0.25	A*	10–1	0.1–0.05
Oceanic upper crust (molten)	12	2900	1000	K_2	T_{S2}	T_{L2}	380	0.25	A*	10–1	0
Oceanic lower crust (solid)	11	3000	1000	K_2	T_{S3}	T_{L3}	380	0.25	B*	10–1	0.3–0.15
Oceanic lower crust (molten)	12	2900	1000	K_2	T_{S3}	T_{L3}	380	0.25	B*	10–1	0
Mantle (solid)	13,14	3300	1000	K_3	T_{S4}	T_{L4}	400	0.022	C* + D*	10–1	0.3–0.15
Mantle (hydrated/serpentinized)	15,16	3300	1000	K_3	T_{S4}	T_{L4}	400	0.022	E* + F*	10–1	0.1–0.05
Mantle (molten)	17	2900	1000	K_3	T_{S4}	T_{L4}	400	0.022	E* + F*	10–1	0
References[g]	–	1,2	1,2	3	6,7	6,7	1,2	1	4,5	–	–

[a] The thermal expansion coefficient $\alpha = 2 \times 10^{-5}\,K^{-1}$ and the compressibility coefficient $\beta = 0.75 \times 10^{-5}\,MPa^{-1}$ are used for all rock types.

[b] $K_1 = (0.64 + 807/(T_K + 77))\cdot\exp.(0.00004P_{MPa})$; $K_2 = (1.18 + 474/(T_K + 77))\cdot\exp.(0.00004P_{MPa})$; $K_3 = (0.73 + 1293/(T_K + 77))\cdot\exp.(0.00004P_{MPa})$.

[c] $T_{S1} = \{889 + 17{,}900/(P + 54) + 20{,}200/(P + 54)^2$ at $P < 1200$ MPa$\}$ or $\{831 + 0.06P$ at $P > 1200$ MPa$\}$; $T_{S2} = \{973–70{,}400/(P + 354) + 778 \times 10^5/(P + 354)^2$ at $P < 1600$ MPa$\}$ or $\{935 + 0.0035P + 0.0000062P^2$ at $P > 1600$ MPa$\}$; $T_{S3} = 1327 + 0.0906P$; T_{S4} = KATZ2003.

[d] $T_{L1} = 1262 + 0.09P$; $T_{L2} = 1423 + 0.105P$; $T_{L3} = 1423 + 0.105P$; T_{L4} = KATZ2003.

[e] Parameters of viscous flow laws are shown in Table 3. Constant viscosity of 10^{18} Pa·s is used for the sticky air and water.

[f] Strain weakening effect is included in the plastic rheology, in which both cohesion C_0 and effective friction coefficient sin(φ_{eff}) decrease with larger strain. The cut-off values are corresponding to the strain '0–1'.

[g] References: 1-Turcotte and Schubert (2002); 2-Bittner and Schmeling (1995); 3-Clauser and Huenges (1995); 4-Ranalli (1995); 5-Karato and Wu (1993); 6-Schmidt and Poli (1998); 7-Katz et al. (2003).

determined from the laboratory experiments (C*, D*, E* and F* in Table 3) (Karato and Wu, 1993).

3.2.2. Plastic deformation

The extended Drucker-Prager yield criterion (e.g., Ranalli, 1995) is implemented as follows:

$$\eta_{\text{plastic}} = \frac{\sigma_{\text{yield}}}{2\dot{\varepsilon}_{II}}$$
$$\sigma_{\text{yield}} = C_0 + P\sin(\varphi_{\text{eff}}) \quad (8)$$

where σ_{yield} is the yield stress; P is the dynamic pressure; C_0 is the residual rock strength at $P = 0$; φ_{eff} is the effective internal frictional angle, which includes the possible pore fluid/melt effects that control the brittle strength of fluid/melt containing porous or fractured media (e.g., Gerya and Meilick, 2011; Li et al., 2010, 2016). Explicitly, fluid/melt decreases the effective internal frictional angle and yield strength. Strain-weakening is accounted for by the plastic rheological model, in which both the cohesion C_0 and effective friction coefficient $\sin(\varphi_{\text{eff}})$ decrease with strain, as shown in Table 4.

3.2.3. Peierls deformation

The Peierls mechanism for deformation by low-temperature and high-stress plasticity is also included (e.g., Kameyama et al., 1999; Karato et al., 2001).

$$\eta_{\text{peierls}} = \frac{1}{2A_{\text{peierls}}\sigma_{\text{II}}}\exp\left(\frac{E+PV}{RT}\left(1-\left(\frac{\sigma_{\text{II}}}{\sigma_{\text{peierls}}}\right)^{p}\right)^{q}\right) \quad (9)$$

where σ_{II} is the second invariant of stress tensor; σ_{peierls} is a stress value that limits the strength of the material ($\sigma_{\text{peiperls}} =$ 9.1 GPa for dry rocks and 2.9 GPa for wet rocks) (Evans and Goetze, 1979; Katayama and Karato, 2008); A_{peierls}, p, and q are experimentally derived material constants ($A_{\text{peierls}} = 10^{7.8}\,\text{s}^{-1}\text{MPa}^{-2}$, $p = 1$, $q = 2$) (Kocks et al., 1975; Katayama and Karato, 2008). In the subduction models, Peierls creep is often activated in the portion of sinking slabs with large stress and low temperature (Katayama and Karato, 2008), which thus may play significant roles in subduction dynamics.

3.2.4. Integrated rheology

The final effective viscosity is defined as the minimum value among the ductile viscosity (η_{ductile}), the plastic equivalent (η_{plastic}), as well as the Peierls viscosity (η_{peierls}) (Ranalli, 1995), which is further controlled by the cut-off values of [10^{18}, 10^{25}] Pa·s.

$$\eta_{\text{eff}} = \min(\eta_{\text{ductile}}, \eta_{\text{plastic}}, \eta_{\text{peierls}}) \quad (10)$$

3.3. Dehydration and water migration

Water plays significant roles in the subduction processes (Li et al., 2015; and references therein), which is numerically tested in the previous models (e.g., Gerya and Meilick, 2011; Quinquis and Buiter, 2014; Liu et al., 2017). It is included in the current numerical models in the forms of both connate water and mineral water. The connate water, present in sediment and oceanic upper crustal basalt of the model, makes up to 1.0 wt% at the surface and decreases to zero at 25 km (Connolly, 2005; Gerya and Meilick, 2011):

$$X_{\text{H}_2\text{O(wt.\%)}} = \left(1 - \frac{\Delta z}{25}\right)X_{\text{H}_2\text{O}(p_0)} \quad (11)$$

where $X_{\text{H}_2\text{O}(p_0)}$ is the connate water content at the surface (1.0 wt%); Δz is the depth below the surface (0–25 km). For the other rock types, e.g., oceanic lower crust, continental crust and mantle, the connate water content is assumed to be negligible.

The mineral-bound water capacity is computed with Perple_X (Connolly, 2005, 2009) as a function of pressure and temperature for four typical rock types in the subduction models, i.e. sediment, basalt (oceanic upper crust), gabbro (oceanic lower crust) and hydrated mantle, with representative compositions summarized in Table 5. The P-T range for the water capacity of sediment is $P_{\text{max}} = 7$ GPa and $T_{\text{max}} = 1500$ °C (Fig. 3a), since the sediment generally cannot be subducted to deeper mantle. In contrast, the water capacities in oceanic crust (basalt, gabbro) and mantle are computed with pressures up to 30 GPa (Fig. 3b-d), i.e. a depth in the lower mantle, which thus allow the simulation of water activity in the whole upper mantle including the MTZ, and even to the topmost lower mantle.

As the subducting slab moves downward, it is going to dehydrate. The release of connate water occurs with increasing depth above 25 km (Eq. 11), which mimics the effects of low-temperature (< 300 °C) reactions that are not included in our thermodynamic databases (Fig. 3). For the calculation of mineral water content, the pressure and temperature changes at each timestep are traced, which will determine the water content of specific rock types following the phase diagram (Fig. 3). Thus, the calculation of connate water is independent of, but complementary to the mineral water.

The propagation of water is modeled in the form of markers: dehydration reactions lead to a release of a certain amount of water, which is stored in a newly generated water marker. Water markers move through the rocks with the following velocity:

Table 5
Model rock compositions (wt%) used for the calculations of water capacity.[a]

	MgO	FeO	CaO	Al_2O_3	Na_2O	K_2O	SiO_2	Reference
Sediment	2.59	5.43	6.21	12.42	2.53	2.13	61.09	(a)
Basalt	7.57	10.42	11.37	14.68	2.78	0.0	50.4	(b)
Gabbro	12.08	6.89	10.74	14.08	1.23	0.0	53.52	(c)
Peridotite	37.44	7.47	3.18	4.03	0.33	0.0	45.55	(d)

[a] The representative compositions of four rock types are, respectively, according to (a) the compiled datasets of global subducting sediment (GLOSS) (Plank and Langmuir, 1998), (b) mean composition of global ocean ridge basalts (Gale et al., 2013), (c) synthetic composition of oceanic lower crustal gabbro (Behn and Kelemen, 2003) and (d) the LOSIMAG-C1 composition of peridotite (Hart and Zindler, 1986). The compositions have been simplified by neglecting the minor elements such as Mn, P, Ti, Cr and the assumption that all Fe is ferrous. In addition, CO_2 has been removed from the GLOSS sediment composition.

Table 6
Mineral phases and thermodynamic data sources for the calculations of water capacity.

Phase	Symbol[a]	Note/Source
Olivine	O(HP)	Holland and Powell, 1998
Orthopyroxene	Opx(HP)	Holland and Powell, 1996
Clinopyroxene	Omph(HP)	Holland and Powell, 1996
Majoritic garnet	Maj	Stixrude and Lithgow-Bertelloni, 2011
Spinel	Sp(HP)	Holland and Powell, 1998
Wadsleyite	Wad	Stixrude and Lithgow-Bertelloni, 2011
Ringwoodite	Ring	Stixrude and Lithgow-Bertelloni, 2011
Magnesiowüstite	Wus	Stixrude and Lithgow-Bertelloni, 2011
Feldspar	feldspar	Fuhrman and Lindsley, 1988
Brucite	B	Ideal
Talc	T	Ideal
Antigorite	Atg(PN)	Padrón-Navarta et al., 2013
Chlorite	Chl(HP)	Holland et al., 1998
White mica	Mica(CHA)	Coggon and Holland, 2002; Auzanneau et al., 2010
Clinoamphibole	GlTrTsPg	Wei and Powell, 2003; White et al., 2003
Phase A	A-phase	Ideal
Clinohumite	Chum	Ideal
Staurolite	St(HP)	Holland and Powell, 1998

[a] The symbols for the mineral phases used as solution models in Perple_X (http://www.perplex.ethz.ch/PerpleX_solution_model_glossary.html).

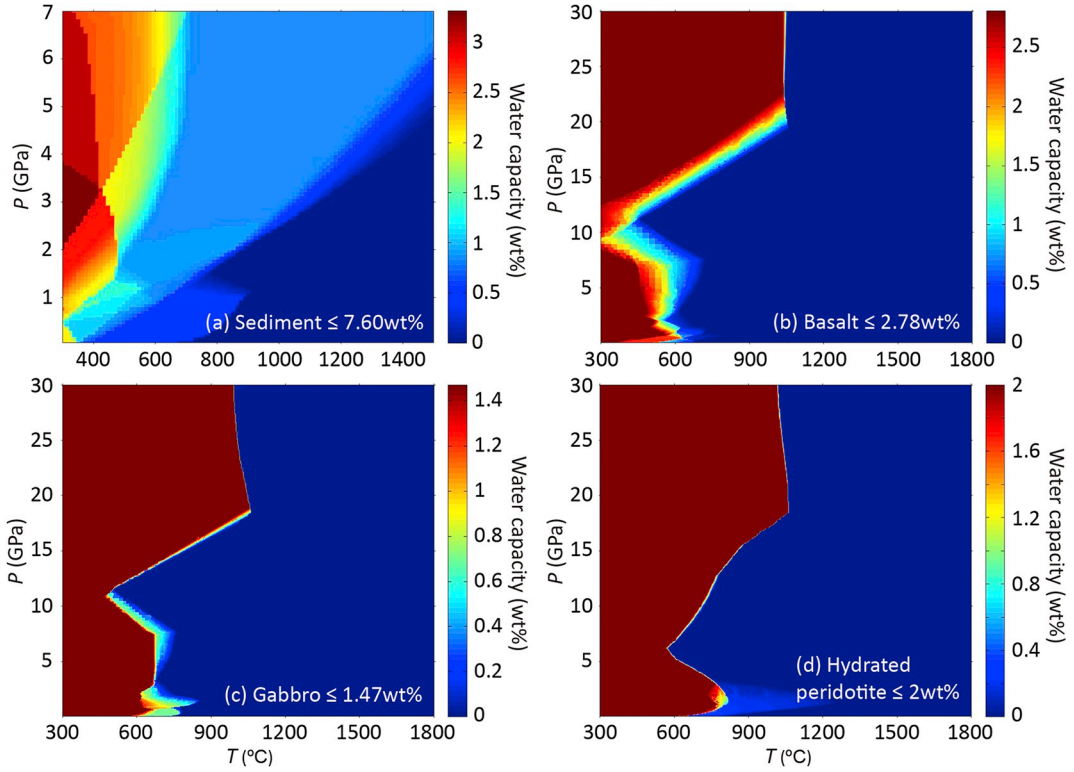

Fig. 3. Computed water capacity for four rock types that constitute the model slab, i.e. sediment (a), basalt/oceanic upper crust (b), gabbro/oceanic lower crust (c), as well as the hydrated peridotite/mantle (d). The representative compositions of these four rock types are compiled in Table 5, which are, respectively, according to the global subducting sediment (GLOSS) (Plank and Langmuir, 1998), the mean composition of global ocean ridge basalts (Gale et al., 2013), the synthetic composition of oceanic lower crustal gabbro (Behn and Kelemen, 2003) and the LOSIMAG-C1 composition of peridotite (Hart and Zindler, 1986). The compositions have been simplified by neglecting the minor elements such as Mn, P, Ti, Cr and the assumption that all Fe is ferrous. In addition, CO_2 has been removed from the GLOSS sediment composition. The phase diagram sections are computed by Perple_X using Gibbs free energy minimization (Connolly, 2005, 2009). The thermodynamic database and equation of state for water are used according to Holland and Powell (1998). The mineral phases and the sources for their solution models used in this study are summarized in Table 6. The maximum water content for each rock type is limited to account for initial incomplete or heterogeneous hydration (Gerya et al., 2006): sediment = 7.60 wt% (a); oceanic upper crust = 2.78 wt% (b); oceanic lower crust = 1.47 wt% (c); hydrated mantle = 2.00 wt% (d). In the thermodynamic calculations (a-d), the water capacity of nominally anhydrous minerals (NAMs) is not included. In order for considering its effect, a minimum water capacity of 0.1 wt % is applied for the mantle rocks (e.g., Faccenda et al., 2012). The mineral water capacity at low-temperature (< 300 °C) is not calculated due to the complex phase transitions, which will be equivalent to the one at 300 °C and the same pressure, when being applied in the geodynamic models.

$$v_{i(\text{water})} = v_i - A\left(\frac{\partial P}{\partial x_i} - g_i \rho_{\text{fluid}}\right)$$
$$A = \frac{v_{\text{percolation}}}{g_2(\rho_{\text{mantle}} - \rho_{\text{fluid}})} \quad (12)$$

where $v_{i(\text{water})}$ is the fluid velocity; v_i is the local velocity of solid rock; A is a water percolation constant with a presumed standard value of $v_{\text{percolation}}$ = 10cm/yr (e.g., Peacock, 1990; Gorczyk et al., 2007; Faccenda et al., 2012); ρ_{mantle} and ρ_{fluid} are the rock and fluid densities, respectively, where ρ_{fluid} is assumed to be 1050 kg/m^3. g_2 = 9.81 m/s^2 is the vertical gravitational acceleration component. When a moving water marker meets a lithology capable of absorbing water by hydration or partial melting reactions at given P–T conditions and rock composition (Fig. 3), the water will be consumed. Properties of crustal rocks are not affected by (de)hydration in our models (Table 4). However, hydration changes properties of the mantle in terms of rheological flow law (hydrated mantle rheology applied independent of actual water content) and the water-content-dependent partial melting (Table 4).

3.4. Partial melting

Partial melting algorithms of both the crustal and mantle rocks are included in the numerical models. For the mantle rocks, the water-content-dependent parameterization of Katz et al. (2003) is applied, which is however limited to the depths of < 300 km, because this model is inaccurate when extending to larger pressure (e.g., Yang et al., 2018a). In the depths of ≥300 km, the partial melting of mantle rocks is not included due to the lack of robust melting models. On the other hand, for a given crustal rock type at a certain pressure, the volumetric degree of melting is assumed to be a linear function of temperature:

$$M = 0, \text{ when: } T \le T_{\text{solidus}}$$
$$M = \frac{(T - T_{\text{solidus}})}{(T_{\text{liquidus}} - T_{\text{solidus}})}, \text{ when: } T_{\text{solidus}} < T < T_{\text{liquidus}}$$
$$M = 1, \text{ when: } T \ge T_{\text{liquidus}} \quad (13)$$

where T_{solidus} and T_{liquidus} are the solidus and liquidus temperatures, respectively, which are specified for each rock type and dependent on the pressure (Table 4) (Schmidt and Poli, 1998; Katz et al., 2003). For a specific rock, when M is larger than zero, it will be considered as partially molten. The marker type of this rock will be changed and then traced during the model evolution.

4. Initial model design

Two-dimensional large-scale numerical models in a Cartesian box of 5000 × 1400 km are applied to study the subduction processes of an oceanic slab as well as its interaction with the MTZ. The spatial resolution of the model is 1 × 1 km in the upper central model domain where the subduction initiates, which gradually changes to 10 × 10 km

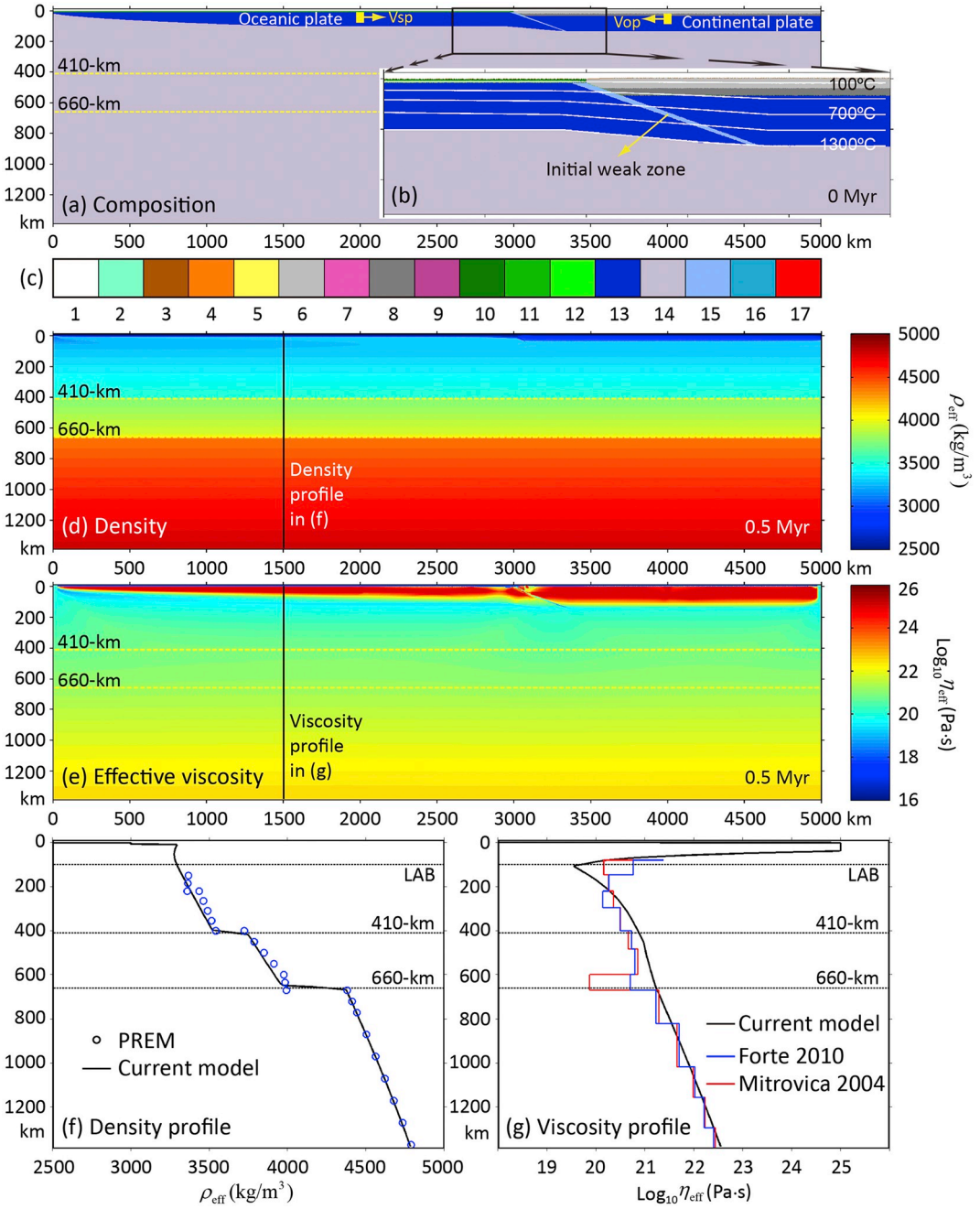

Fig. 4. Initial model setup. (a) Composition field in the framework of 5000 × 1400 km, in which the 410 km and 660 km discontinuities are shown with yellow dashed lines. (b) The enlargement of initial subduction zone, with an oceanic plate on the left, a continental plate on the right and an initial weak zone in between. The white lines are shown for isotherms, starting from 100 °C with the interval of 300 °C. The colors in (a) and (b) indicate for rock types as specified by the colorbar in (c): 1- sticky air; 2-water; 3,4-sediment; 5-partially molten sediment; 6-continental upper crust; 7-partially molten continental upper crust; 8-continental lower crust; 9-partially molten continental lower crust; 10,11-oceanic upper and lower crust, respectively; 12-partially molten oceanic crust; 13,14-lithospheric and subjacent mantle, respectively; 15,16-hydrated and serpentinized mantle, respectively; 17-partially molten mantle. In the numerical models, some rocks/layers share the same properties or physical laws for their calculation, with different colors used for visualizing internal deformation and structural development. This is the case for sediments (3 and 4 in Figure c), lithospheric and asthenospheric mantles (13 and 14 in Figure c), as well as the hydrated and serpentinized mantles (15 and 16 in Figure c). Detailed properties of different rock types are shown in Table 4. In addition, the partially molten oceanic upper and lower crusts share the same colour (12 in Figure c) for visualization, but with different properties for simulation as shown in Table 4. The main reason is that the oceanic crust is rather thin, the partially molten of which is rather limited. Thus we do not want to use an additional colour to distinguish them. It is also worth noting that some rock types, e.g., sediment and partially molten rocks are not shown in the initial model, but will appear during the evolution of the model (e.g., Fig. 6). (d) The density structure of the model domain, with a vertical profile as shown in (f). The modeled density is compared to the sub-lithospheric mantle density from the Preliminary Reference Earth Model (PREM; blue circles in (f)) (Dziewonski and Anderson, 1981). (e) The effective viscosity field of the model, with a vertical profile as shown in (g). The modeled effective viscosity is compared to the sub-lithospheric mantle viscosity inferred from the joint inversions of glacial isostatic adjustment (GIA) data as well as the global convection-related observables (Mitrovica and Forte, 2004; Forte et al., 2010). (For interpretation of the references to colour in this figure legend, the reader is referred to the web version of this article.)

in the regions far away from it, similarly to Gerya et al. (2008) and Li (2014). In addition, > 20 million active Lagrangian markers are used to trace the internal lithological boundaries, material properties, etc.

4.1. Initial compositional and thermal structures

The model mainly comprises two domains (Fig. 4a, b): an oceanic plate on the left and a continental plate on the right, with an initial weak zone in between. The oceanic lithosphere is composed of a 3 km thick basalt layer as the upper crust, a 5 km thick gabbro layer as the lower crust, as well as a mantle layer with the thickness dependent on the age of the lithosphere. The continental lithosphere is set up by a 20 km thick upper crust, a 15 km thick lower crust and a mantle layer with variable thicknesses. The initial weak zone between the oceanic and continental lithospheres is about 10 km thick on the top and 5 km thick at the bottom of the lithospheric mantle, which is used to locate the initial convergence. The rheological properties of hydrated mantle are applied for the weak-zone material as shown in Fig. 4.

On the top of the model domain, a 'sticky air' layer with low density and viscosity is applied (Schmeling et al., 2008; Crameri et al., 2012), which allows the direct calculation of topography evolution, i.e. the spontaneous deformation of the crustal surface. According to the isostatic equilibrium, the initial thickness of sticky air layer is 10 km above continent and 12 km above oceanic crust. Crameri et al. (2012) found that the sticky air approach is adequate as long as the term $(\eta_{st}/\eta_{ch})/(h_{st}/L)^3$ is small, where η_{st} and h_{st} are the viscosity and thickness of the sticky air layer, and η_{ch} and L are the characteristic viscosity and length scale of the model, respectively. According to this criterion, the quality of the internal free-surface condition in the current models is rather moderate.

The initial thermal structure of continental lithosphere is laterally uniform with a linear gradient defined by 0 °C at the surface and 1350 °C at the bottom of lithospheric mantle (white lines in Fig. 4b). The initial thermal structure of oceanic lithosphere is defined by the half-space cooling model and thus controlled by its age (e.g., Turcotte and Schubert, 2002). The initial thermal gradient in the sub-lithospheric mantle is about 0.5 °C/km.

4.2. Phase transitions and density structure

The phase transitions at 410 km and 660 km discontinuities are included in the numerical models (e.g., Bina and Helffrich, 1994; and references therein), which modify the mantle density structure (Fig. 4d) in addition to the gradual pressure and temperature dependence (Eq. 2). In the current study, these phase transitions are only affecting the density, whereas the related variations of latent heat and possible viscosity change are not considered. For the phase transition at around 410 km, we implement a linear 0–6% increase in density from the P-T-dependent spinel-in line (here implemented at $P_{MPa} = (T_K–1758) \times C_{410} + 13{,}400$) to the P-T-dependent olivine-out line (here implemented at $P_{MPa} = (T_K–1758) \times C_{410} + 13{,}600$). On the other hand, for the phase transition at around 660 km, we implement a linear 0–10% increase in density from the P-T-dependent perovskite-in line (here implemented at $P_{MPa} = (T_K–1883) \times C_{660} + 22{,}800$) to the P-T-dependent spinel-out line (here implemented at $P_{MPa} = (T_K–1883) \times C_{660} + 23{,}000$). The resulted density jumps of the mantle are consistent with the Preliminary Reference Earth Model (PREM) (Fig. 4f) (Dziewonski and Anderson, 1981). The Clapeyron slopes of these phase transitions play crucial roles in modifying the density structure of subducting slab and thus affecting the slab and MTZ interaction. The values of the Clapeyron slopes at 410 km and 660 km discontinuities are widely studied based on the laboratory experiments (e.g., Katsura and Ito, 1989; Ito and Takahashi, 1989; Ito et al., 1990); however, they are still not well constrained. The summary of experimentally derived data indicates that $C_{410} \in (1.5,\ 3.6)$ MPa/K and $C_{660} \in (-4.0,\ -0.4)$ MPa/K, both of which occupy wide ranges of values (Tables 1 and 2). In the reference model of this study, the normal values of 3.0 MPa/K and −3.0 MPa/K are applied for the 410 km and 660 km discontinuities, respectively. As comparisons, the effects of variable values of Clapeyron slopes, covering the whole possible parameter range, are also systematically studied.

Besides the aforementioned phase transitions, two additional effects are also included, i.e. the oceanic crustal eclogitization (Ito and Kennedy, 1971, 2013) and the metastable olivine in the MTZ (Rubie and Ross, 1994), which could both influence the density structure of the subducting slab. For the eclogitization, we implement a linear 0–16% increase in density from the P-T-dependent garnet-in line (the basalt to garnet granulite transition, here implemented at $P_{kbar} = 0.014 \times T_{°C}$ -5.4) to the P-T-dependent plagioclase-out line (the garnet granulite to eclogite transition, here implemented at $P_{kbar} = 0.020 \times T_{°C} + 4.0$). Thus, the density increase coefficient varies from 0 to 0.16 between these lines (Ito and Kennedy, 1971, 2013). The algorithm of eclogitization is described and systematically tested in Sizova et al. (2015). For the metastable olivine, according to the experimental results of Rubie and Ross (1994), we implement a transitional temperature range from 550 °C to 700 °C, which controls the olivine to wadsleyite phase transition. If the temperature of portions of sinking slab is lower than 550 °C in the MTZ, the phase change does not occur in this region, i.e. the density jump from olivine to wadsleyite will not be applied in the very cold core of slab. In contrast, if the temperature of sinking slab is higher than 700 °C in the MTZ, the phase change and density jump from olivine to wadsleyite occurs instantaneously. Between 550 °C and 700 °C, the linear interpolation of density increase of sinking slab in the MTZ is applied. On the other hand, recent experiments also reveal the possible ultraslow phase transition of pyroxene to garnet in the subducting slab with low temperature (Van Mierlo et al., 2013), which is however not applied in the current models.

4.3. Effective viscosity structure

The rheology of the subduction model is controlled by the competing viscous, plastic and Peierls strengths for specific rock types at external conditions with certain pressure, temperature, stress and strain rate (Section 3.2; Tables 3 and 4). The resulting effective viscosity structure (Fig. 4e, g) demonstrates strong top lithosphere and weak asthenosphere, as well as the slowly increasing viscosity in the MTZ and uppermost lower mantle. The rheological profile is generally consistent with the sub-lithospheric mantle viscosity inferred from the joint inversions of glacial isostatic adjustment (GIA) data as well as the global convection-related observables (Fig. 4g) (Mitrovica and Forte, 2004; Forte et al., 2010). A significant difference is the thin, weak layer at the bottom of the MTZ in some of the joint inversion models (e.g., red line in Fig. 4g; Mitrovica and Forte, 2004), which may be due to the grain size reduction and/or superplasticity (e.g., Karato, 2008) and might play significant roles in the slab flattening (Mao and Zhong, 2018). The weak layer is not included in the reference models; however, its effects on the slab/MTZ interaction will be systematically tested. In addition, no prescribed viscosity jump is applied at the 660 km discontinuity in the reference models, the effects of which will also be tested.

4.4. Boundary conditions

For the velocity boundary condition, free slip is satisfied for all boundaries. In addition, both the subducting and overriding plates are pushed internally by constant convergence velocities in the yellow squares as shown in Fig. 4a, which produces approximately uniform velocity of the horizontally moving plates. The convergence velocity is applied for subduction initiation, and will be cancelled after 10 Myrs in the reference model, leaving the subduction process driven purely by the internal buoyancy, i.e. self-consistently.

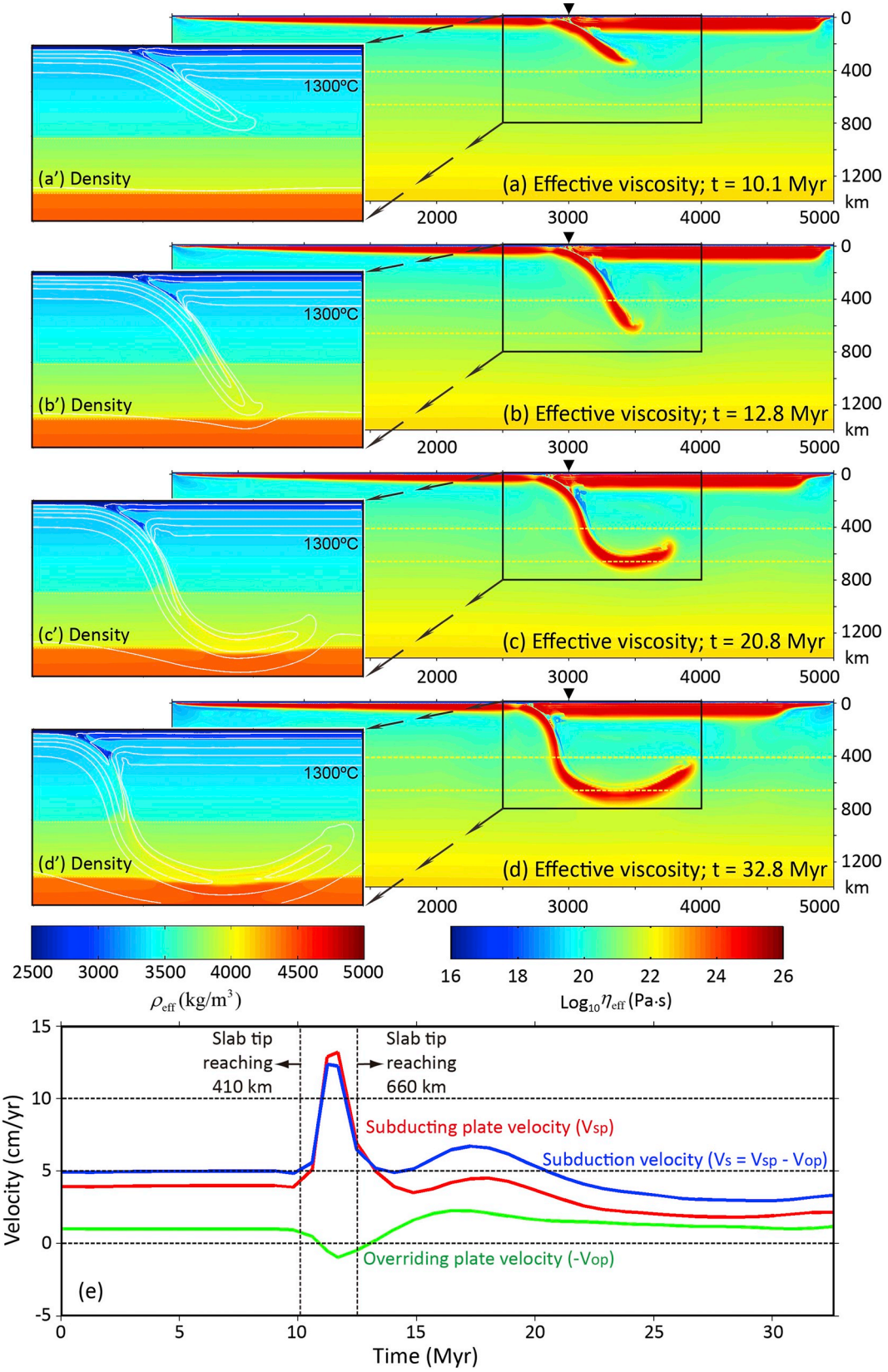

(caption on next page)

Fig. 5. The reference model evolution, with the effective viscosity shown in the right column (a-d) and density in the left column (a′-d′). The white lines are shown for isotherms, starting from 100 °C with the interval of 300 °C. The black inverted triangle on top of the viscosity filed indicates the initial position of the trench. The initial age of the oceanic plate is from 0 Ma to 60 Ma. The thickness of continental plate is 140 km. The Clapeyron slopes of phase transitions at 410 km and 660 km discontinuities are 3.0 MPa/K and −3.0 MPa/K, respectively. The initial convergence velocity is 5 cm/yr, with the subducting plate pushed rightward by Vsp = 4 cm/yr and the overriding plate pushed leftward by Vop = −1 cm/yr (e). The position of pushing is shown in Fig. 4a. The prescribed velocities are cancelled after 10 Myrs. Then the subduction system is driven purely by its own buoyancy. The kinematic evolutions of converging plates are shown in (e), with red line for subducting plate velocity (Vsp), green line for overriding plate velocity (-Vop) and blue line for the whole subduction velocity (Vs = Vsp-Vop). The subducting and overriding plate velocities are measured in the positions about 500 km from the far-end tips of the converging plates, respectively. The overriding plate velocity is similar to the trench velocity, due to the rather limited deformation of overriding plate. (For interpretation of the references to colour in this figure legend, the reader is referred to the web version of this article.)

For the thermal boundary condition, fixed values of 0 °C and 1975 °C are applied for the top and bottom boundaries, respectively. The horizontal heat flux across the vertical boundaries is zero.

5. Reference model results

In the reference model, the initial cooling age of the oceanic plate increases from 0 Ma at the left end to 60 Ma at the prescribed subduction initiation zone. The thickness of continental lithosphere is 140 km, i.e. a moderate value of natural continental plate. The initial convergence velocity is 5 cm/yr, with the oceanic plate pushed rightward by Vsp = 4 cm/yr and the continental plate pushed leftward by Vop = −1 cm/yr, which will be cancelled after 10 Myrs. Then the subduction system is driven purely by its own buoyancy. The Clapeyron slopes of phase transitions at 410 km and 660 km discontinuities are 3.0 MPa/K and − 3.0 MPa/K, respectively. The initial model configuration and detailed parameters are shown in Fig. 4 as well as Tables 3 and 4.

The model results show that the subduction velocity is significantly increased when the sinking slab passing through the 410 km discontinuity and entering the MTZ (Fig. 5a, e). This is mainly attributed to the positive Clapeyron slope of 410 km phase transition which increases the density of subducting slab, although it can be kinetically delayed in the very cold core of the slab (Fig. 5b′). Later, when the slab sinks through the MTZ and reaches the 660 km discontinuity, the subduction velocity decreases to ~5 cm/yr (Fig. 5b, e), due to the resistance from the negative Clapeyron slope of 660 km phase transition. Afterwards, the slab is bent anticlockwise and flattens at the bottom of MTZ (Fig. 5c-d). During the transition from generally straight (Fig. 5b) to bent slab (Fig. 5c), the subduction velocity increases to a peak value of ~7 cm/yr, due to a reduction in the resistance from the 660 km discontinuity on the vertical slab, which phenomenon has also been observed in the previous models (e.g., Čížková and Bina, 2013). Finally, the slab keeps flattening in the MTZ with continuous trench retreating of 1–2 cm/yr, during which the subduction has a stable velocity of ~3 cm/yr (Fig. 5c, d, e).

The rate of plate advance is always larger than the trench retreating rate in the reference model (Fig. 5e), which is consistent with the natural observations that rollback velocities are commonly < 50% of the total subduction velocity (e.g., Lallemand et al., 2005; Sdrolias and Müller, 2006). Capitanio et al. (2007) proposed two factors for enhancing plate advance, i.e. low viscosity asthenosphere and ridge push. Accordingly, the significant Earth-like plate advancing in the current model should be controlled by the low viscosity on the top of the asthenosphere (Figs. 5 and 4g).

Besides the general styles and kinematics of subduction, the numerical model also demonstrates the material transportation and fluid/melt activities in the subduction channel (Fig. 6). During slab sinking into the hot mantle, the water is released from the oceanic crust and migrates upward, which further hydrates the overriding mantle wedge (Fig. 6b-e). Most water of the subducting crust is lost above the depths of ~150 km, whereas a certain amount of water is carried up to 250 km (Fig. 6b′-e′). However, very limited amount of water of the oceanic crust is taken deeper than 250 km or even to the MTZ. The model also shows a hydrated mantle layer carried into the MTZ, with a thickness of several tens of kilometers above the subducting slab (Fig. 6c-e). The water-content of this weak layer, which is controlled by the prescribed water capacity of nominally anhydrous minerals (NAMs), is low (≤0.1 wt%). The high temperature of this mantle layer results in decompositions of the hydrous minerals, which thus locates in the blue domain of Fig. 3d with only limited water content in NAMs. The water activity and hydration process can decrease the solidus temperature of mantle peridotite, which results in significant partial melting in the sub-arc depth (Fig. 6b-e). The melt fraction is > 4% in the core of this partially molten region (Fig. 6c″-e″). Thus, the magmatism in the island arc could be expected, although the melt extraction process is not directly simulated in the current models.

The hydration and partial melting play significant roles in the decoupling of converging plates and thus facilitate continuous subduction processes. For comparison, a test model with neither hydration nor partial melting is shown in Fig. S1 in the Supporting information. It indicates very strong coupling between the subducting and overriding plates. Consequently, the subduction ceases when the initial pushing velocity is cancelled. Two additional models are further conducted with testing the effects of oceanic crustal eclogitization and metastable olivine, respectively (Figs. S2 and S3 in the Supporting information). In the model without crustal eclogitization, the self-consistent trench retreat velocity is negligible and the subduction velocity is decreased, which thus only result in short slab flattening in the MTZ (cf. Figs. S2 and 5). It indicates that the decreased slab pull due to the absence of crustal eclogitization hinders trench retreat and hinders the continuously long slab flattening in the MTZ (Fig. S2). In the model without the effect of metastable olivine, the general subduction evolution is similar to the reference case (cf. Figs. S3 and 5). The main difference is the higher peak subduction velocity of > 15 cm/yr when the sinking slab entering the MTZ (Fig. S3e), which indicates that metastable olivine can regulate very fast subduction. For example, if subduction is rapid, then the temperature of the slab will be low and contribute to the formation of metastable olivine. The delay of phase transition and density jump will lead to slower subduction, which thus regulate the subduction kinematics.

6. Subduction mode selection during slab and MTZ interaction

6.1. Dependence on the Clapeyron slopes of 410 km and 660 km phase transitions

The Clapeyron slopes at 410 km and 660 km discontinuities are still not well constrained, both of which occupy wide ranges of values according to the laboratory experiments (Tables 1 and 2).

Four sets of numerical models are firstly conducted with variable Clapeyron slopes (Fig. 7). In the first model with low Clapeyron slopes for both 410 km and 660 km discontinuities, i.e. C_{410} = 1 MPa/K and C_{660} = −1 MPa/K (Fig. 7a), the induced forces by these phase transitions on the subducting slab are relatively small comparing to other similar models with larger C_{410} and/or C_{660}. Thus the slab will easily penetrate the MTZ and enter the lower mantle, during which the subduction kinematics is generally stable with negligible trench retreat (Fig. 7a, a′). In the second model with the same low C_{660} = −1 MPa/K but increased C_{410} = 4 MPa/K (Fig. 7b), the slab can still penetrate the

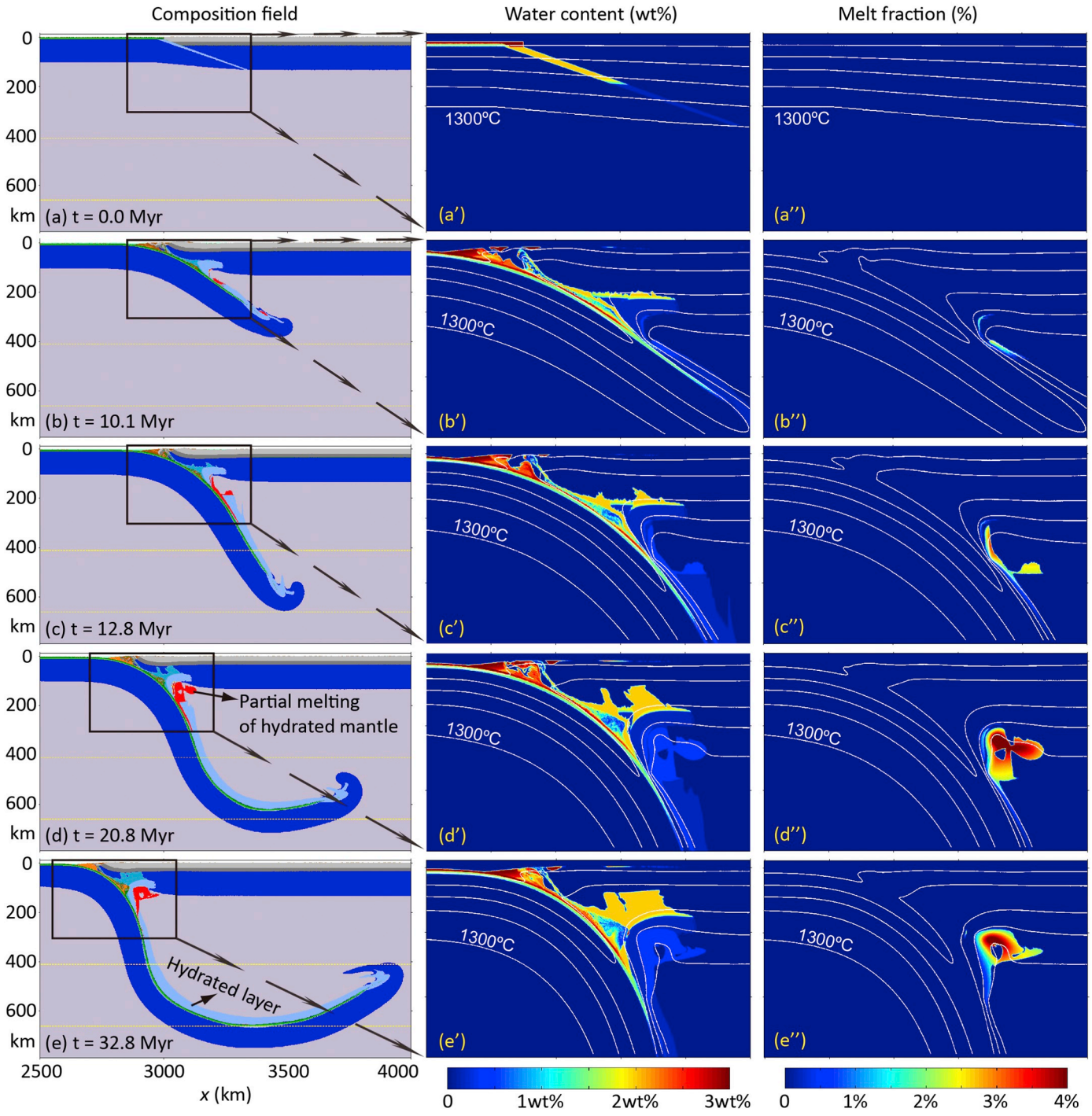

Fig. 6. The reference model (same as Fig. 5) evolution, with the composition field shown in the left column (a-e), water content in the middle column (a′-e′) and melt fraction in the right column (a″-e″). The colors in the composition field (a-e) represent the rock types as shown in Fig. 4c. White lines in the water content (a′-e′) and melt fraction fields (a″-e″) show the isotherms, starting from 100 °C with the interval of 300 °C.

MTZ easily, due to the low resistance at 660 km. However, the subduction has a peak high velocity to ~15 cm/yr when slab passing through the 410 km, which indicates the significant density and drag force increase by the high positive Clapeyron slope 'C_{410}' (Fig. 7b′). In addition, the trench is retreating with a velocity of ~1 cm/yr during the subduction, which is thus different from the model with low C_{410} (Fig. 7a′). The sinking slab tends to flatten at ~1000 km depth in both of the models (Fig. 7a, b). This slab behavior looks similar to some geophysical observations (Fukao and Obayashi, 2013); however, the similarity should be considered with caution due to the possible effects of free-slip lower boundary condition applied at 1400 km in the current models.

In the third model with low C_{410} = 1 MPa/K but high C_{660} = −4 MPa/K (Fig. 7c), the subducting slab does not penetrate the 660 km discontinuity but instead stagnates in the MTZ, due to the strong resistance by the phase transition at 660 km. During the slab stagnation process, the subduction velocity is generally low with 2–3 cm/yr, and the trench motion is negligible (Fig. 7c′). In the fourth model with high Clapeyron slopes for both 410 km and 660 km discontinuities, i.e. C_{410} = 4 MPa/K and C_{660} = −4 MPa/K (Fig. 7d), the

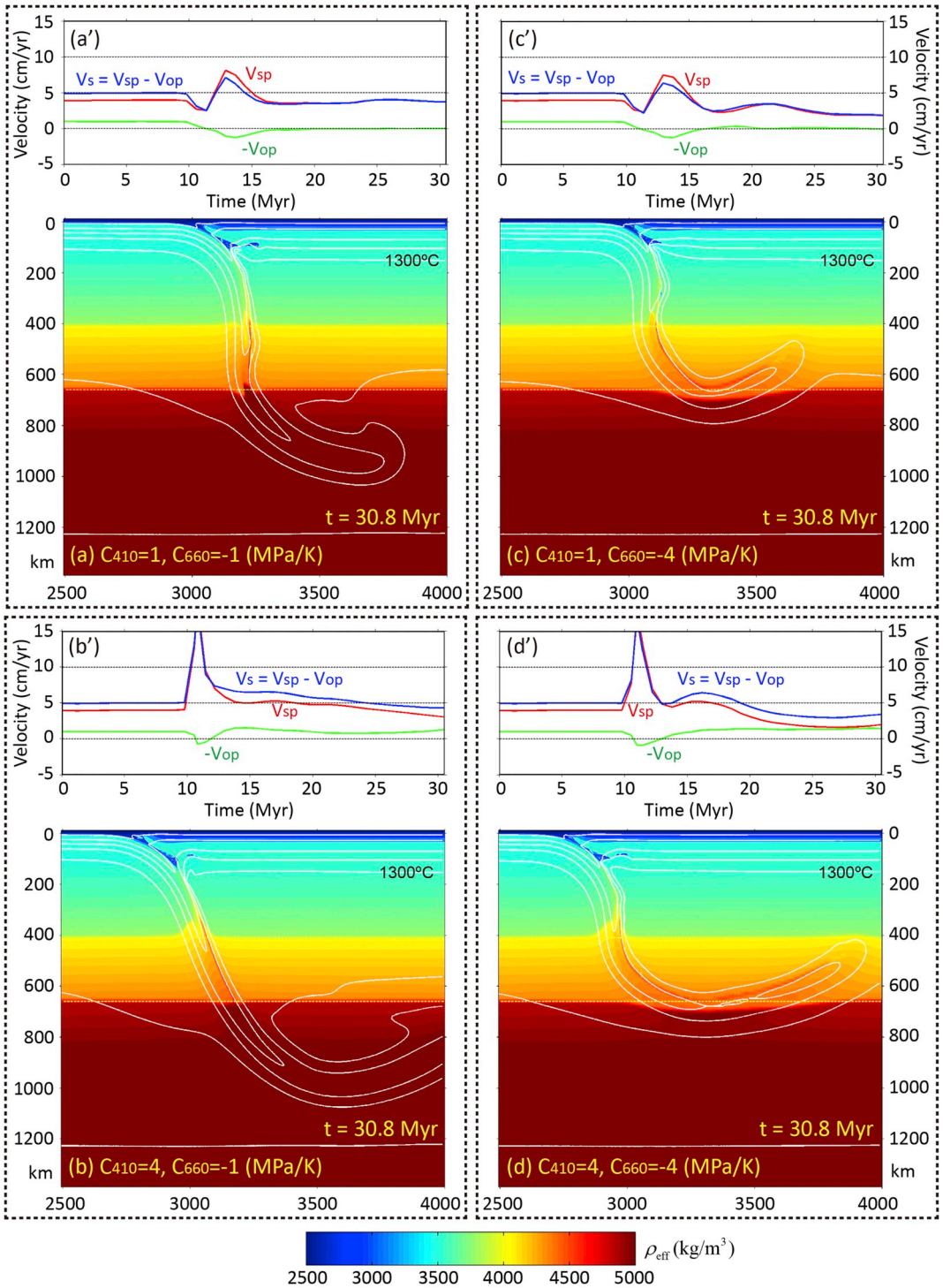

Fig. 7. Model results with four different sets of Clapeyron slopes for 410 km and 660 km phase transitions as shown in each Figure (a-d). All the other parameters are identical to the reference model (Figs. 5-6). The colors in (a-d) indicate the density, with the colorbar shown at the bottom. The white lines are shown for isotherms, starting from 100 °C with the interval of 300 °C. (a′-d′) The kinematic evolutions of converging plates, with red line for subducting plate velocity, green line for overriding plate velocity and blue line for the whole subduction velocity. (For interpretation of the references to colour in this figure legend, the reader is referred to the web version of this article.)

subducting slab does not penetrate into the lower mantle but flattens in the MTZ, again mainly due to the large resistance by the 660 km phase transition. In addition, the high Clapeyron slope of 410 km phase transition leads to significant and continuous trench retreat with a velocity of ~2 cm/yr (Fig. 7d′), which contributes to the long (~1000 km) slab flattening in the MTZ (Fig. 7d).

Based on the comparisons among the kinematics of these models, it indicates that the high value of C_{410} results in a significant increase of subduction velocity directly after the cancellation of prescribed convergence (i.e. 'pushing') at 10 Myr (Fig. 7b′, d′). In contrast, a decrease of subduction velocity is firstly resulted after the pushing in the models with low value of C_{410} (Fig. 7a′, c′), which is then followed by an increase of subduction velocity. As we know, the Clapeyron slope C_{410} is defined by the $\triangle P/\triangle T$, in which P and T are pressure and temperature,

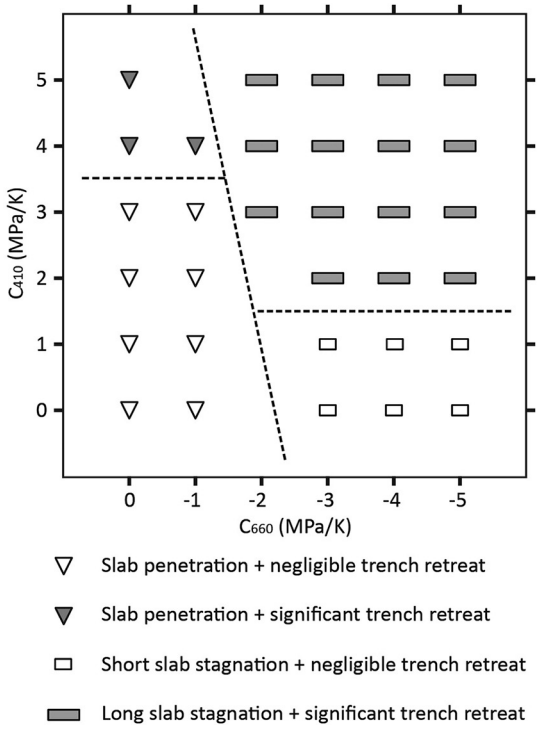

Fig. 8. Regime diagram of subduction mode selection in the MTZ, with variable values of Clapeyron slopes for the 410 km and 660 km phase transitions. All the other parameters are identical to the reference model (Figs. 5-6). Long slab stagnation is defined as that around 1000 km as in Fig. 7d. In contrast, the short stagnant slab is around 500 km as in Fig. 7c.

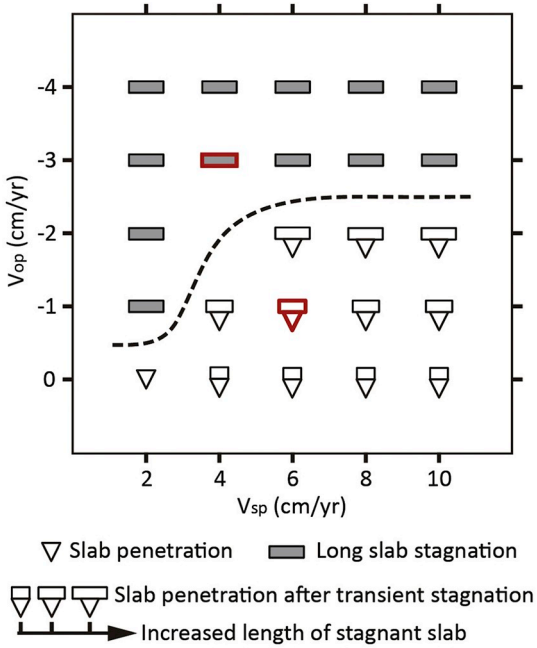

Fig. 9. Mode selection of slab and MTZ interaction with variable plate convergence velocities. The prescribed velocities for subducting plate (Vsp) and overriding plate (Vop) are kept constant during the whole model evolution. All the other parameters are identical to the reference model (Figs. 5–6). The model evolutions of two representative experiments with red symbols are further shown in Fig. 10. (For interpretation of the references to colour in this figure legend, the reader is referred to the web version of this article.)

respectively, for the phase transition. For a sinking slab, the lower temperature condition will contribute to the phase change at a lower pressure, due to the positive C_{410}. On the other hand, the sinking slabs arrive at a similar depth of ~400 km, with a similar thermal structure (i.e. similar ΔT), after 10 Myrs in these four different models, comparable to Fig. 5a. Thus, the higher value of C_{410} results in phase change at lower pressure, in which condition the density of the slab tip is increased with producing faster subduction (Fig. 7b′, d′). Alternatively, in the models with low value of C_{410}, the phase transition and density increase of the slab tip do not occur, which thus leads to a slowdown of subduction after the cancellation of pushing (Fig. 7a′, c′). Further on, when the slab tip reaches the 410 km discontinuity with phase change and density increase, the subduction will speed up.

Systematic numerical models are further conducted with variable Clapeyron slopes of 410 km and 660 km phase transitions, the results of which are summarized in a regime diagram (Fig. 8). It indicates that the Clapeyron slope at 660 km (C_{660}) controls the mode selection of slab penetration or stagnation. In the regime with $|C_{660}| > 2$, the slab stagnation is generally predicted. Alternatively, the penetration mode dominates with low values of $|C_{660}| \leq 1$. The Clapeyron slope of C_{410} plays significant roles in affecting the trench motion. In the regime of slab penetration, the high values of $C_{410} \geq 4$ will lead to significant trench retreat. In contrast, the trench is quite stable with relatively low values of $C_{410} \leq 3$. In the regime of slab stagnation, the higher values of $C_{410} \geq 2$ result in long slab (around 1000 km as in Fig. 7d) flattening in the MTZ with significant trench retreat. However, the stagnant and flattened slab is relatively short (around 500 km as in Fig. 7c), due to the negligible trench retreat in the models with $C_{410} \leq 1$.

6.2. Dependence on the kinematics of the converging plates

In order to better understand the mode selection, a series of models are conducted with prescribed variable subducting and overriding plate velocities which keep constant during the whole model evolution (Fig. 9). The model results demonstrate that the high trench retreating velocities of ≥3 cm/yr generally result in long slab stagnation and flattening in the MTZ (Figs. 9, 10a). In addition, the relatively slow trench retreat (1–2 cm/yr) will also lead to long slab stagnation when the advancing velocity of subducting plate is also low (e.g., 2 cm/yr). Alternatively, the mode of slab direct penetration or penetration after short stagnation will be finally resulted in the models with slow or none trench retreat and faster subducting plate advance (Figs. 9, 10b).

6.3. Dependence on the age/thickness of the converging plates

Besides the kinematics of converging plates, their age/thickness may also affect the slab mode selection in the MTZ. In order to further study the combined effects, systematic numerical models are constructed (Fig. 11).

In the kinematic regime with stable overriding plate (Vop = 0) and relatively fast subducting plate motion (Vsp = 6 cm/yr) for the entire model evolution, only two similar modes are predicted, i.e. the direct penetration or penetration after short stagnation (Fig. 11a). It indicates that the slab prefers penetration to the lower mantle in such a regime with no trench retreat. The age of subducting plate (Asp) and thickness of overriding plate (Dop) can only slightly modify the mode selection, in which the thicker overriding plate and intermediate slab age tend to result in transient short slab stagnation before the final penetration (Fig. 11a).

In the kinematic regime with the same total convergence rate (Vs = Vsp – Vop = 6 cm/yr), but a slow trench retreat (Vop = −1 cm/yr), the model results can be divided into three domains (Fig. 11b). With older subducting slab and thinner overriding plate, the penetration mode is predicted, whereas the thicker overriding plate contributes to transient slab stagnation before the penetration. Compared to the models with stable trench (Fig. 11a), the trench retreat with just a low rate slightly promotes the slab stagnation in the MTZ, which results in

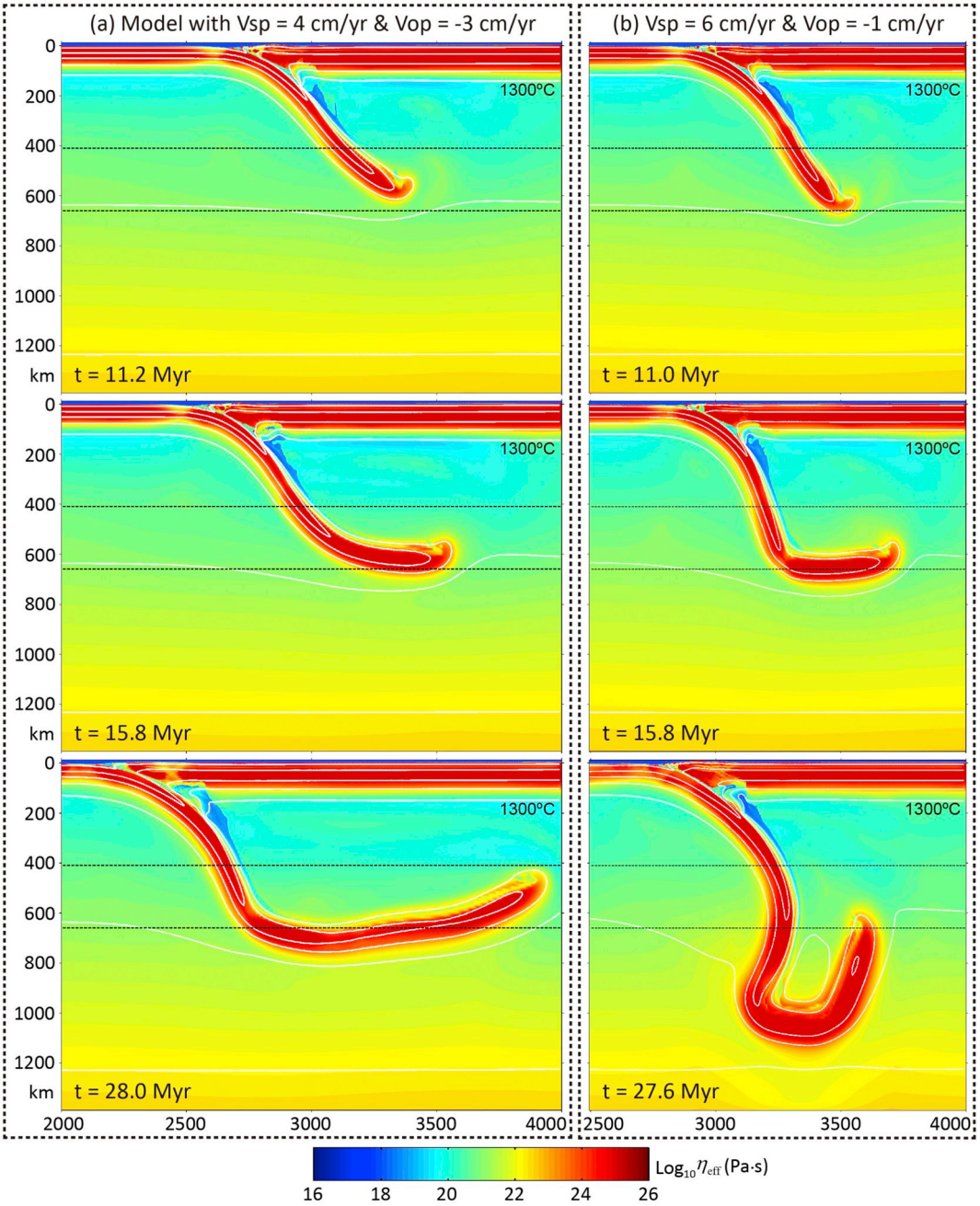

Fig. 10. Two representative model evolutions from Fig. 9 (red symbols). Both models have the same total convergence velocity of 7 cm/yr; however, the partition between subducting and overriding plates is different as shown on top of each model. The colors indicate the effective viscosity, with the colorbar shown at the bottom. The white lines are shown for isotherms, starting from 100 °C with the interval of 300 °C. (For interpretation of the references to colour in this figure legend, the reader is referred to the web version of this article.)

an additional domain with transient long slab stagnation before the penetration (Fig. 11b).

In the kinematic regime with relatively fast trench retreat (Vop = −2 cm/yr) and the same total convergence rate of 6 cm/yr, the stable long slab stagnation mode is resulted with thick overriding plate (Fig. 11c). The domain of penetration mode is significantly decreased, which only appears in the top-left corner with old subducting slab and thin overriding plate. In the transition domain, a transient style of slab stagnation is resulted before the final penetration. Based on the comparison among the three sets of models with different kinematic conditions, it indicates again that the increase of trench retreat can gradually promote slab stagnation in the MTZ.

In the above three groups of models, the prescribed convergence velocity is kept constant during the whole model evolution (Fig. 11a-c). As comparisons, an additional kinematic regime is conducted, in which the prescribed velocities (Vsp = 5 cm/yr, Vop = −1 cm/yr) will be cancelled after the slab tip reaching ~400 km (Fig. 11d). The choice of this boundary condition is, on one hand, generally consistent with the reference model in Fig. 5a, in which the slab tip is approaching ~400 km after the prescribed convergence of 10 Myrs. On the other hand, the slab pull in this situation will be large enough for driving continuous subduction with a reasonable velocity of several cm/yr. The model results demonstrate that slab penetration is strongly controlled by the thinner overriding plate (Fig. 11d), in which case the slab sinks sub-vertically through the MTZ into the lower mantle, which then curves backward due to the return flow on the left side of the model

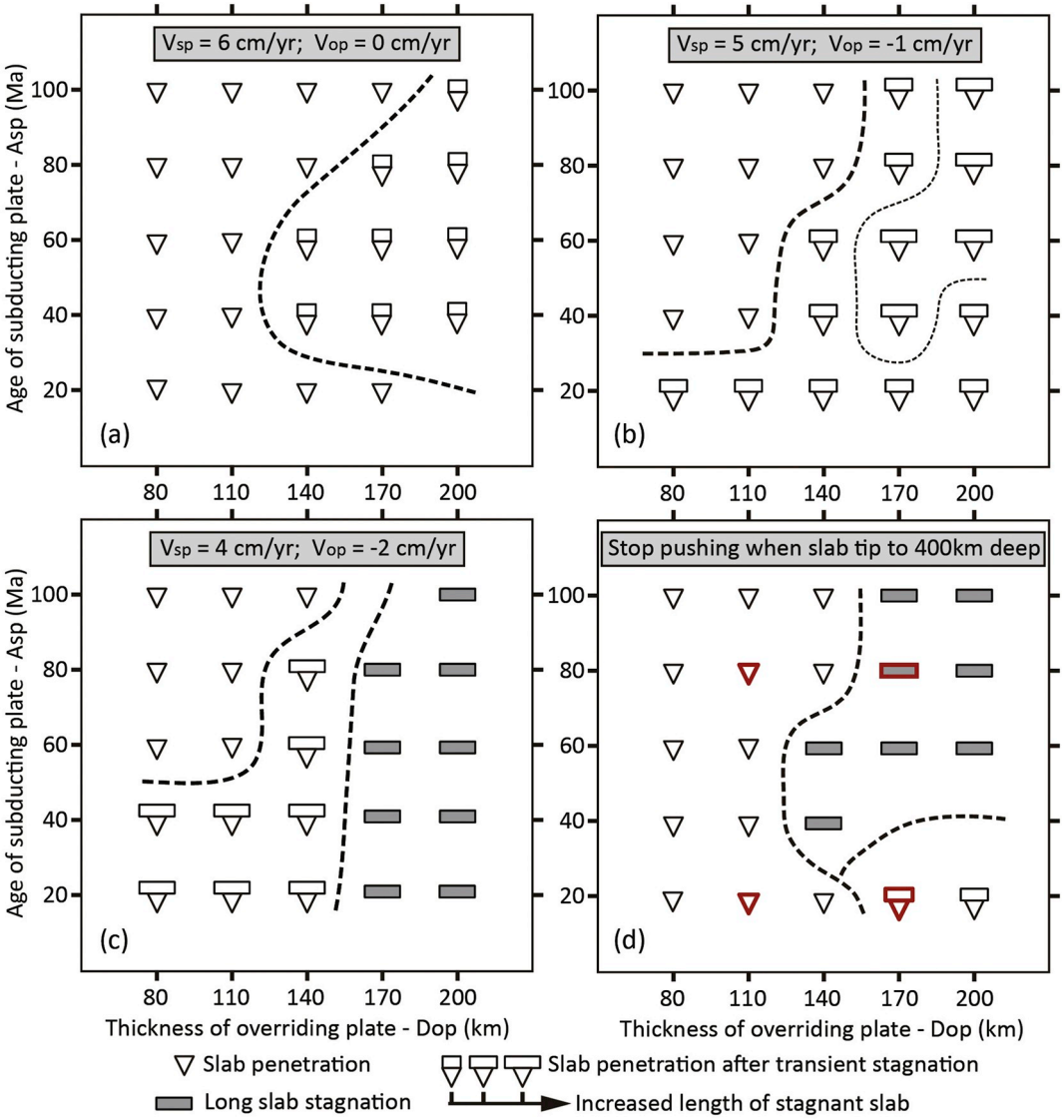

Fig. 11. Mode selection of slab and MTZ interaction with variable ages of subducting plate (Asp) and thicknesses of overriding plate (Dop), in different kinematic regimes with variable convergence velocities as shown on the top of each diagram. The prescribed velocities will be kept constant during the whole model evolution in the diagrams (a)-(c). In contrast, the prescribed pushing velocities, i.e. Vsp = 5 cm/yr and Vop = −1 cm/yr, will be cancelled after the slab tip reaching ~400 km in the diagram (d). All the other parameters are identical to the reference model (Figs. 5–6). The model evolutions of four representative experiments with red symbols in (d) are further shown in Fig. 12. (For interpretation of the references to colour in this figure legend, the reader is referred to the web version of this article.)

domain induced by the subducting slab (e.g., Fig. 12a, b). In these cases, the subduction kinematics is rather stable with a velocity of ~5 cm/yr and negligible trench motion, except at the time when slab tip passing through 410 km discontinuity (Fig. 12a′, b′). On the other hand, the long slab stagnation mode is resulted in the models with a thicker overriding plate and a subducting slab that is not younger than 40 Ma (Fig. 11d). In this situation, the resulted shallow slab angle and significant trench retreat contribute to the slab flattening in the MTZ (Fig. 12c, c′). Finally, in the remaining domain with thick overriding plate (170–200 km) and young subducting slab (20 Ma), transient slab stagnation is predicted before the final penetration (Fig. 11d). In this case, the young and deformable slab, accompanied by a transient trench retreat (10–20 Myr in Fig. 12d′), results in a stage of slab flattening in the MTZ (Fig. 12d). However, the trench retreat stops afterwards, with slab dip angle increasing to be sub-vertical, which finally leads to slab penetration to the lower mantle (Figs. 12d, d′).

As a summary, the models indicate that the influence of overriding plate thickness on the slab/MTZ interaction is strongly coupled with the slab dip angle and trench motions (Figs. 11, 12). In the regime with constant convergence velocities (e.g., Fig. 11a-c), the thick overriding plate leads to shallower dip angle of the sinking slab in the upper mantle, which further contributes to the slab (transient) stagnation. Alternatively, with free subduction after the initial pushing, the thickness of overriding plate takes effects by modifying the trench motions (Fig. 12). For example, thick overriding plate, accompanying with older subducting slab, leads to significant trench retreat (cm/yr), which will further result in long slab stagnation in the MTZ (Fig. 12c, c′).

In another aspect, the effects of subducting slab age are not very clear from Fig. 11. It seems that, with prescribed plate and trench velocities (e.g., Fig. 11b-c), the old slabs penetrate more easily, at least for the cases with thinner overriding plate. Under these conditions, the old sinking slab is stronger and thus can penetrate through the MTZ more easily than the young slab that is deformable when interacting with the 660 km discontinuity. On the other hand, with free plate motions, older subducting slabs beneath thicker overriding plate lead to shallower dip angle and more trench retreat, which in turn causes stagnation.

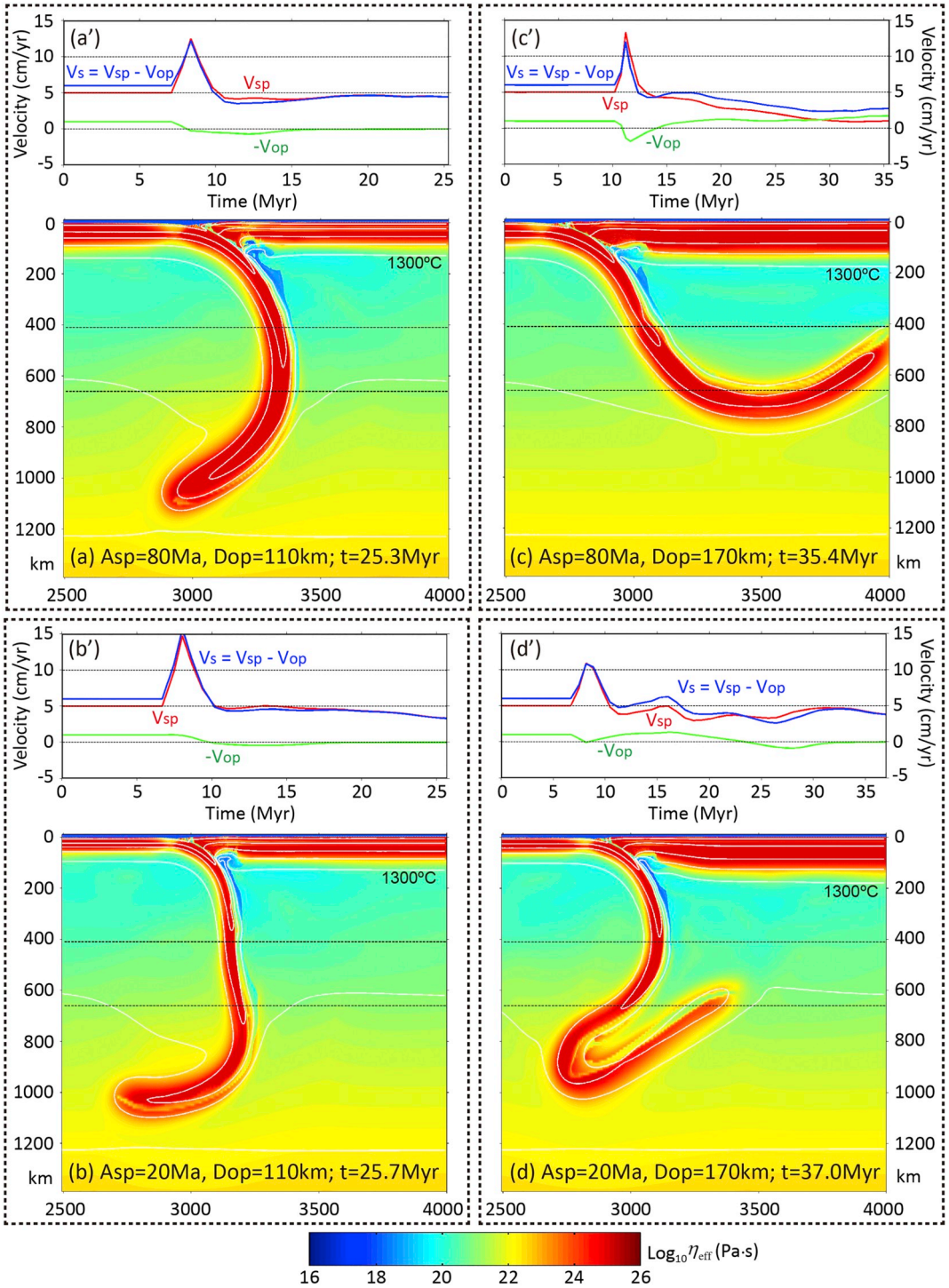

Fig. 12. Four representative models from Fig. 11d (red symbols), with variable ages of the subducting slab (Asp) and/or thicknesses of the overriding plate (Dop) as shown in the Figures (a–d). The colors in (a–d) indicate the effective viscosity, with the colorbar shown at the bottom. The white lines are shown for isotherms, starting from 100 °C with the interval of 300 °C. (a′-d′) The kinematic evolutions of converging plates, with red line for subducting plate velocity, green line for overriding plate velocity and blue line for the whole subduction velocity. (For interpretation of the references to colour in this figure legend, the reader is referred to the web version of this article.)

However, with thinner overriding plate, the resulted steep subducting slab with negligible trench retreat can easily penetrate the MTZ (Fig. 12a, a′, b, b′).

6.4. *Effect of a thin, weak layer at the bottom of MTZ*

A thin, weak layer at the bottom of MTZ is proposed in some of the joint inversion models (Fig. 4g) (e.g., Mitrovica and Forte, 2004), which is not included in the aforementioned numerical simulations. In this section, the effects of such a weak layer, which is 50 km thick (610–660 km in depth) and has a constant viscosity of 10^{20} Pa·s, are numerically tested for the experiments in Fig. 8 with variable Clapeyron slopes at 410 km and 660 km discontinuities. The results demonstrate that the existence of such a weak layer does not change the mode

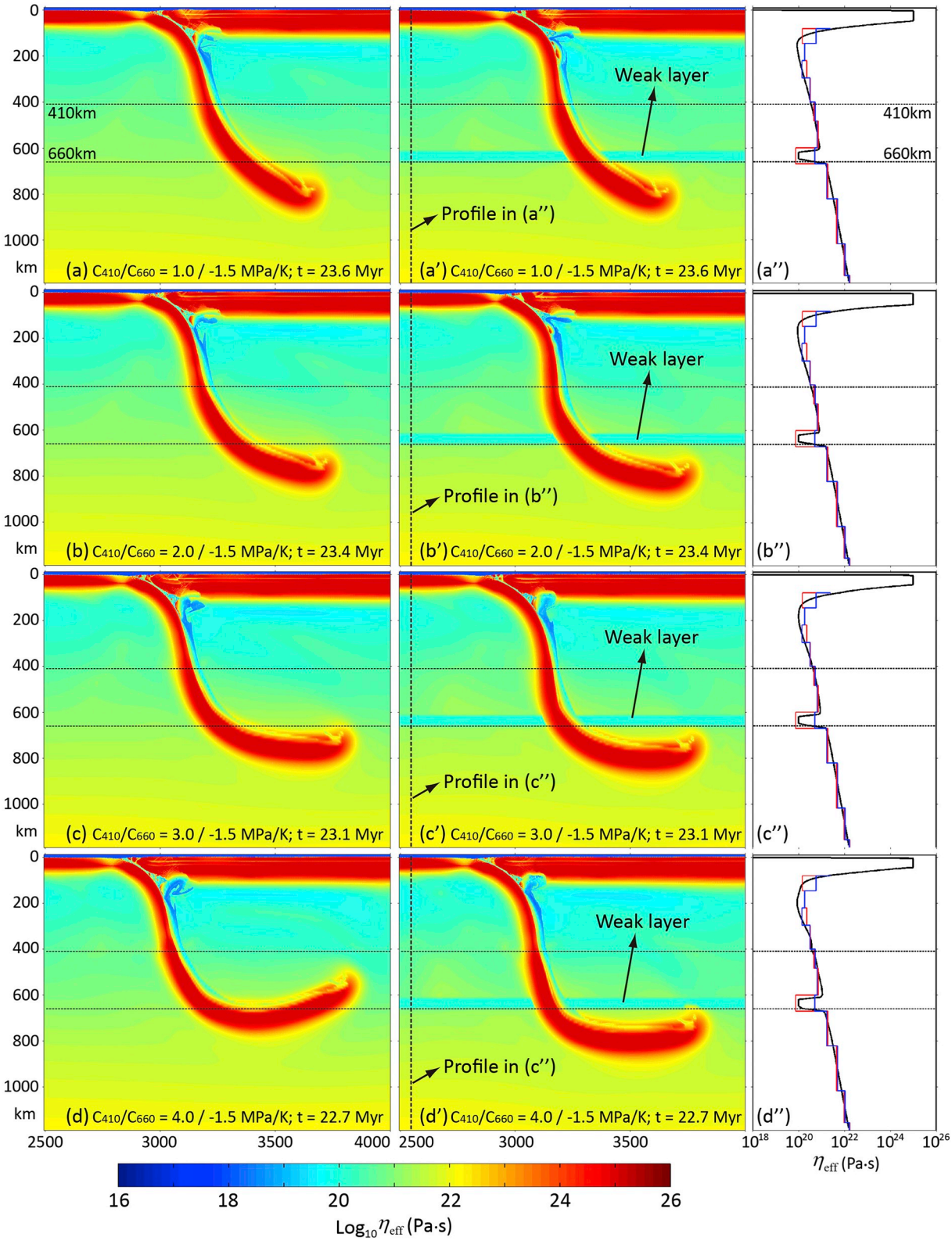

Fig. 13. Comparisons between models without (a-d) and with (a′-d′) a weak layer at the bottom of the MTZ. (a-d) Four numerical models with variable Clapeyron slopes of 410 km phase transition (C_{410} = 1, 2, 3, or 4 MPa/K). Instead, the same Clapeyron slope is applied at 660 km, i.e. C_{660} = −1.5 MPa/K, which represents the transition between slab penetration and stagnation modes as shown in Fig. 8. (a′-b′) Four numerical models comparable to those in (a-d), respectively, but with a weak layer at the bottom of MTZ. (a″-d″) The effective viscosity profiles of the numerical models in (a′-d′). The modeled effective viscosity (black line) is compared to the sub-lithospheric mantle viscosity profiles inferred from the joint observations (red and blue lines; same as in Fig. 4g) (Mitrovica and Forte, 2004; Forte et al., 2010). (For interpretation of the references to colour in this figure legend, the reader is referred to the web version of this article.)

selection between penetration and stagnation (detailed results not shown here), although it may slightly affect the slab geometry.

Further on, an additional set of models are conducted with a transitional Clapeyron slope between slab penetration and stagnation modes as shown in Fig. 8, i.e. $C_{660} = -1.5$ MPa/K, which may imply the most sensitive condition for slab mode selection in the MTZ. The results show that the weak layer does not significantly modify the slab morphology in the models with lower C_{410} (cf. Fig. 13a and a′, b and b′). In contrast, the existence of a weak layer can change the slab mode from stagnation into penetration in the model with higher Clapeyron slope of $C_{410} = 4.0$ MPa/K (cf. Fig. 13d and d′). Actually, it is the only model we have conducted in which the slab mode selection is switched due to the existence of a weak layer at the bottom of MTZ (Fig. 13d and d′). Based on the summary of model results, this weak layer can slightly promote the slab penetration through the MTZ, which indicates that the sub-vertical regime boundary in Fig. 8 may be shifted only a little bit rightward if including such a weak layer. Thus, the rather limited effect of the weak layer implies that the reference viscosity structure of the current study (Fig. 4g) is valid for exploring the dynamics of slab/MTZ interaction.

6.5. Effect of a sharp viscosity jump at 660 km discontinuity

The average viscosity of lower mantle is generally considered to be one to two orders higher than that of the upper mantle (e.g., Hager, 1984) as discussed in Section 1. In the aforementioned numerical models with self-consistently calculated visco-plastic-Peierls rheology, the effective viscosity of upper mantle is about $10^{19.5}$–10^{21} Pa·s, whereas the lower mantle is about 10^{21}–$10^{22.5}$ Pa·s (Figs. 4g and 14a). The simply averaged viscosity ratio between lower and upper mantle is about 30, which is thus consistent with the general estimations (10–100). A sharp viscosity jump at the 660 km discontinuity is not prescribed in the aforementioned models; however, it is widely applied in the previous studies (e.g., Agrusta et al., 2017; Crameri and Lithgow-Bertelloni, 2018). For comparisons, we further conduct a series of numerical models with variable constant viscosity of the lower mantle (Fig. 14a). The rheology of crust and upper mantle is still calculated with the combined visco-plastic-Peierls flow laws (Eqs. (6)–(10)).

The systematic model results indicate that the lower mantle viscosity jump and Clapeyron slope of 660 km phase transition (C_{660}) can both promote the slab stagnation in the MTZ (Fig. 14b). If the viscosity of lower mantle is low ($\eta_{LM} = 10^{21}$ Pa·s), the sinking slab always penetrates through the 660 km discontinuity, even with high $|C_{660}| = 4$ MPa/K. In contrast, if $\eta_{LM} = 10^{23}$ Pa·s, the slab stagnation occurs exclusively, even with negligible $|C_{660}| = 0$ MPa/K. With intermediate values of η_{LM}, slab stagnation is predicted with higher $|C_{660}|$, whereas slab penetration occurs with lower $|C_{660}|$. In addition, the constant viscosity of $\eta_{LM} = 10^{22}$ Pa·s can be approximately regarded as the average value of the gradually increased lower mantle viscosity in the reference model (Figs. 4g and 14a). The slab mode selection with constant $\eta_{LM} = 10^{22}$ Pa·s and variable C_{660} (Fig. 14b) agrees well with the corresponding models with a viscosity-depth gradient, i.e. a horizontal line of models with $C_{410} = 3$ MPa/K in Fig. 8. It indicates that a viscosity-depth gradient has a similar effect with an averaged sharp viscosity jump between the lower and upper mantles.

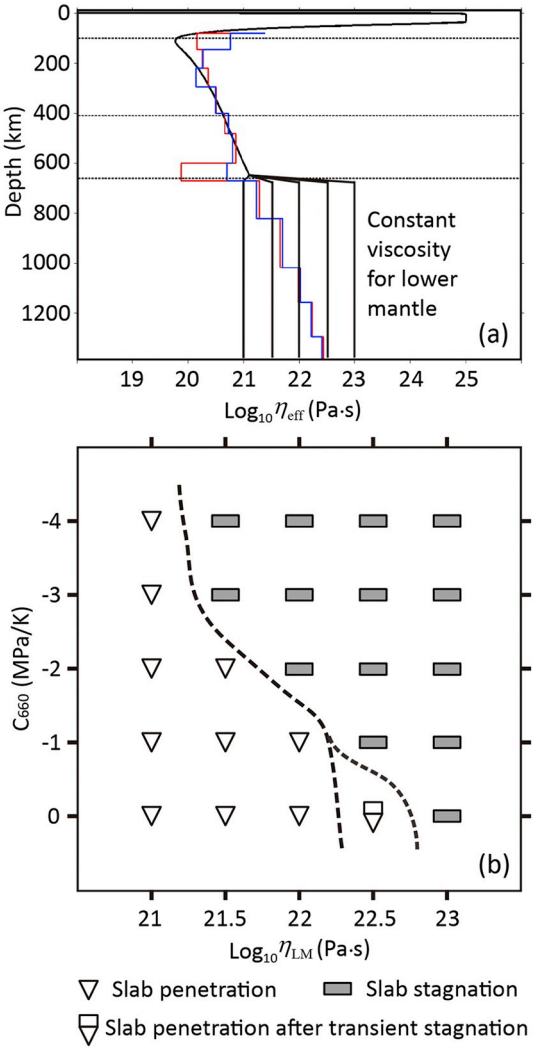

Fig. 14. Numerical models with prescribed constant viscosity of the lower mantle (η_{LM}). (a) Effective viscosity profiles (black lines) with $\eta_{LM} = 10^{21}$, $10^{21.5}$, 10^{22}, $10^{22.5}$ and 10^{23} Pa·s, respectively. The red and blue lines (same as in Fig. 4g) represent the sub-lithospheric mantle viscosity profiles inferred from the joint observations (Mitrovica and Forte, 2004; Forte et al., 2010). (b) Slab mode selection in the MTZ with variable constant viscosity of the lower mantle (η_{LM}) and variable Clapeyron slopes of 660 km phase transition (C_{660}). The Clapeyron slope at 410 km discontinuity ($C_{410} = 3$ MPa/K) and all the other parameters are identical to the reference model in Fig. 5. (For interpretation of the references to colour in this figure legend, the reader is referred to the web version of this article.)

7. Discussion

7.1. Slab/MTZ interaction and comparisons with previous models

The dynamics of subducting slab and MTZ interaction has been investigated in a number of previous models (e.g., Billen, 2010; Čížková and Bina, 2013; Garel et al., 2014; Agrusta et al., 2014, 2017; Holt et al., 2015; King et al., 2015; Crameri and Lithgow-Bertelloni, 2018; Shi et al., 2018; Yang et al., 2018b), which applied different model setups, boundary conditions as well as the rheology and density structures. These studies significantly improve our understanding of the subducting slab mode selection and its interaction with the MTZ.

The previous numerical studies are mostly based on pure mechanical or thermomechanical models, in which a weak oceanic crust with variable thickness (e.g., 5–20 km) is generally applied in order for the decoupling of subducting and overriding plates (e.g., Čížková and Bina, 2013; Garel et al., 2014; Holt et al., 2015; Agrusta et al., 2017). In the current models, thermodynamic database of deep water activity (Fig. 3) is integrated into the thermomechanical models, which thus allows the hydration weakening of the subduction channel. Thereby, normal properties of oceanic crust are applied (Ranalli, 1995). The model comparisons indicate that the effects of hydration and partial melting play significant roles in the subduction dynamics (cf. Fig. 5 and Fig. S1 in the Supporting information). In addition, the integrated thermodynamic and thermomechanical models are not only comparable to the large-scale geophysical phenomena, but also to the geological/

petrological processes during subduction, e.g., (de-)hydration, partial melting and magmatism (Fig. 6).

In our previous models without water and melt activities (Shi et al., 2018), an unrealistic cold and strong mantle wedge is generally resulted due to the strong coupling between the converging plates, which occurs similarly in some other models (e.g., Čížková and Bina, 2013; Agrusta et al., 2017). It is resolved in the current models with integrating fluid/melt simulation, which will hydrate the mantle wedge and result in weakening and partial melting there. It is thus consistent with the natural observations. On the other hand, the long slab stagnation mode is not observed in our previous models (Shi et al., 2018), due to the fixed overriding plate and stable trench, which agrees to the current models with similar configurations (Fig. 11a). Another difference is that the previous study predicts a special mode with slab turning backward when touching the 660 km discontinuity, which favors older subducting slab, thinner overriding continent, faster convergence, as well as the high Clapeyron slope of 660 km phase transition (i.e. $C_{660} = -4$ MPa/K) (Fig. 9 in Shi et al., 2018). This backward turning of slab in the MTZ is not observed in the current studies, which may be explained by the initial convergence boundary conditions on both sides of the model. The trench retreat thus leads to lower dip angle of the slab than that in Shi et al. (2018) which is kinematically driven from only the subducting plate side. The hydration weakening of sinking slab and subduction channel may also contribute to the absence of backward slab turning. In such cases, the slab cannot keep its bent morphology, but instead is stretched sub-vertically, favoring penetration through the 660 km discontinuity.

The effects of Clapeyron slopes of 410 km (C_{410}) and 660 km (C_{660}) phase transitions are also investigated in several previous studies (e.g., Čížková and Bina, 2013; Agrusta et al., 2017; Yang et al., 2018b), which generally agree that the large values of C_{660} play significant roles in the slab stagnation. The current studies clearly demonstrate that the relatively high Clapeyron slope of 660 km phase transition controls the slab stagnation in the MTZ (Fig. 8). In addition, the value of C_{410} does not change the mode selection significantly, but will modify the length of flattened slab in the MTZ by affecting the trench motions (Figs. 7-8). Higher values of C_{410} promote trench retreat, which will facilitate the long slab flattening in the MTZ in the cases with also higher C_{660} and the resulting slab stagnation. As one of the few studies that testing the effects of C_{410}, Čížková and Bina (2013) indicates that the higher values of C_{410} will hamper trench retreat, which is thus opposite to the current model results. Based on the comparisons between these two studies, the main difference is that the slab is rather weak in Čížková and Bina (2013), which could be easily deformed and folded in short wavelength. In contrast, the slab is generally stronger in the current study, in which the slab folding is more difficult (Fig. 7). The different rheological properties might be the main cause of the contrasting predictions for the effect of C_{410} on trench motion, which thus require further systematic studies.

Some previous models without Clapeyron slope at 660 km discontinuity (C_{660}), but applying a significant viscosity jump between lower and upper mantles, also predict slab stagnations in the MTZ (e.g., Garel et al., 2014; Holt et al., 2015). The effects of C_{660} and viscosity jump are systematically compared in this study (Fig. 14), which indicate that both of them can promote slab stagnation in the MTZ. It further reveals that a gradually increasing viscosity of lower mantle has a similar effect with an averaged sharp viscosity jump.

The effects of trench motions on the slab stagnation in MTZ are widely accepted, which indicate that the fast trench retreat can significantly promote the slab flattening in the MTZ (e.g., Capitanio et al., 2007; Agrusta et al., 2017; Goes et al., 2017; Yang et al., 2018b). The current models are thus consistent with the previous studies in this aspect, which again demonstrate the significance of trench retreat on the long slab flattening in the MTZ (Figs. 9–10). The trench motions can be controlled by the properties of the converging plates, as well as the far field boundary conditions, e.g., the sea-ward movement of the overriding continent driven by the large-scale mantle convection (e.g., Yang et al., 2018c).

The age of sinking slab may play a significant role in affecting the slab/MTZ interaction. Several previous models indicate that the slab stagnation in the MTZ favors older slabs, which lead to faster trench retreat (e.g., Garel et al., 2014; Agrusta et al., 2017; Yang et al., 2018b). On the other hand, if the trench is fixed, the older slab with higher strength will instead encourage penetration (e.g., Zhong and Gurnis, 1994; Arredondo and Billen, 2016). In the current models with variable ages of subducting slab in the free subduction regime (Fig. 11d), the long slab flattening is observed in the models with older sinking slab and relatively thick overriding continent (i.e. > 140 km), which is thus consistent with the previous models. However, if the overriding continent is thin, e.g. ≤ 110 km, the slab penetration is generally predicted (Fig. 11d). It indicates that the slab mode selection in the MTZ is also affected by the thickness of the overriding plate, which is previously studied in several numerical models (e.g., Capitanio et al., 2007, 2010; Garel et al., 2014; Holt et al., 2015). Capitanio et al. (2007) suggested that the buoyancy and suction of the overriding plate could enhance the trench retreat and shallow the slab dip, which will contribute to the slab flattening in the MTZ. Holt et al. (2015) shows that the overriding plate thickness does not significantly modify the slab stagnation mode if the overriding plate can move freely, in which case the trench retreat dominates. However, if the far end of the overriding plate is held fixed, the thicker overriding plate leads to stable trench and slab vertical folding and penetration, whereas the thinner overriding plate can be stretched with trench retreat and thus facilitate the slab flattening in the MTZ (Holt et al., 2015). The current systematic studies demonstrate that the larger thickness of overriding plate could generally contribute to the slab stagnation and flattening in the MTZ (Fig. 11), in the regimes with variable trench motions, which is thus consistent with the previous study (e.g., Capitanio et al., 2007). It has to be emphasized that the trench retreat is still one of the most critical factors for slab flattening in the MTZ, while the properties of converging plates can also play certain roles (Fig. 11).

The effects of a thin, weak layer at the bottom of MTZ is recently studied with a global mantle convection model, which indicates that this weak layer controls the formation of stagnant slabs in the MTZ and other slab structures in the lower mantle (Mao and Zhong, 2018). They also propose that trench retreat plays an important role in causing slab stagnation in the MTZ. The question is whether this weak layer promotes the trench retreat, or leads to slab sliding at the bottom of the MTZ, both of which may contribute to the slab flattening. According to the regional subduction dynamic models with a single slab performed here, the effect of the weak layer is not crucial, which can only slightly promote slab penetration under the most favorable conditions as shown in Fig. 13. The contrasting results, between the pure dynamic model with a single subduction zone (Fig. 13) and the global mantle convection model driven by time-dependent surface plate motion history (Mao and Zhong, 2018), require further comparable studies.

Concerning the timescale of stagnant slab in the MTZ, Goes et al. (2017) proposed that slabs do not stagnate for > 60 Myrs. In this study, we focus on the relatively short model periods (around 30 Myrs), in which the comparable transient characteristics of slab stagnation are not considered.

7.2. Implications for the complex subduction mode selection in the Earth's MTZ

The slab morphologies in the natural subduction zones are summarized in Fig. 1, with compiling several important parameters that might affect the slab/MTZ interaction, e.g., present-day subducting plate and trench velocities, amount of trench retreat during the past ~50 Ma, slab age in the present trench, as well as the approximated slab dip angle in the upper mantle.

In the aspect of trench motions, the present-day trench velocity does

not have clear correlation with the slab morphology in the MTZ; however, the total trench retreat during the past ~50 Ma seems to have a certain correlation with the slab style (Fig. 1) (Goes et al., 2017). In the subduction zone with large amount of trench retreat (> 1000 km), the long slab flattening in the MTZ is generally observed, e.g., Honshu, Kuriles, Tonga, and so on. There are two exceptions with large trench retreat, but no clear slab flattening in the MTZ, i.e. the Java and Antilles. For the Java subduction zone, a flat slab is observed in the topmost lower mantle, which might represent the sinking of previously flattened slab in the MTZ. For the Antilles subduction zone, this absence of slab flattening may be related to the neighboring Cocos subduction with an opposite direction. On the other hand, the slab penetration mode is generally observed with low value (< 500 km) of trench retreat, e.g., the Cocos, Peru, Bolivia and Hellenic subduction zones. It is worth noting that the slab modes in the MTZ are not clear in several subduction zones with limited trench retreat, e.g., the Alaska, Kamchatka and Sumatra. Finally, in the subduction zones with intermediate trench retreat (500–1000 km), either mode could occur depending on other factors, e.g., slab penetration in Kermadec with trench retreat of ~850 km, but slab flattening in Chile with trench retreat of ~700 km, and so on. The general rule from the observations is thus consistent with the numerical models, in which the fast trench retreat contributes significantly to the slab flattening in the MTZ (Figs. 9 and 10). However, this rule is not always valid (e.g., the Java and Antilles subduction zones in Fig. 1), since many other factors may also influence.

In the aspect of slab age, no clear rules are obtained from the current studies with variable prescribed boundary conditions (Fig. 11), although it indeed can affect the slab/MTZ interaction. Several previous free subduction models indicate that older slab prefers stagnation and flattening in the MTZ (e.g., Garel et al., 2014; Agrusta et al., 2017). According to the observations, most of the flattened slabs in the MTZ are corresponding to the relatively old subducting slab in the trench (blue slabs in Fig. 1). However, several contrasting results are also observed with younger slab subducting and flattening in the MTZ, e.g., Cascadia, Chile and Aleutians subduction zones, which indicate the joint influences of other factors. On the other hand, the young slabs penetrate through the MTZ in several subduction zones, e.g., the Cocos, Peru and Bolivia (green slabs in Fig. 1), whereas the older slabs could also penetrate directly to the lower mantle, e.g., the Kermadec and Hellenic subduction zones. As a summary, the subduction mode selection in the MTZ cannot be solely explained by the slab age.

In the aspect of overriding plate thickness, the model results demonstrate that thicker overriding plate tends to facilitate the slab flattening in the MTZ (Fig. 11) by decreasing the slab dip angle and enhancing the trench retreat. However, no correlations could be built between the slab morphology in the MTZ and the overriding plate thickness in nature, because this thickness is changing through time, e.g., back-arc spreading/compression. Its original value is hard to constrain, which is thus not included in the compilation of Fig. 1. This situation prevents the direct comparisons, between numerical models and natural subduction zones, on the effects of overriding plate thickness.

7.3. Model limitations and future perspectives

The main limitation of the current and most of the previous numerical models is the 2D regime, which thus prevents the toroidal flow around the lateral edges of the subducting slab (Schellart et al., 2011; Li et al., 2014). It might affect, in a certain degree, the trench motions and further the subduction mode selection in the MTZ. The influences of three dimensionality on the slab/MTZ interaction are uncertain, which thus call for large-scale models with 3D spherical geometry in the future. The neglected latent heat of phase changes may also play a role in the slab-MTZ interaction, which should be further investigated.

8. Conclusions

High-resolution thermomechanical numerical models are integrated with the thermodynamic database of water capacity in a large range of pressure and temperature conditions which cover the whole upper mantle and the topmost lower mantle. It thus allows the dynamic simulation of not only the slab subduction processes, but also the coupled water and partial melting activities. Systematic numerical models are conducted to investigate the dynamics of subduction mode selection in the MTZ, which are further compared with the multiple datasets of global subduction zones on the Earth. The main conclusions from this comprehensive study include the following:

(1) The integrated water activity and partial melting contribute to the weakening of subduction channel, the decoupling of converging plates, as well as the forming of a hot and weak mantle wedge beneath the island arc, which is thus consistent with the natural observations.
(2) Generally, from observations and numerical modeling, the favorable conditions of slab stagnation in the MTZ include old/cold lithosphere subducting into the mantle with high Clapeyron slopes at 410 km and 660 km discontinuities, as well as the resulting significant trench retreat and shallow dip angle (Fig. 2). However, these dynamic, kinematic and geometric conditions are often not achieved together for specific subduction zones (Fig. 1), which precludes finding a unique controlling factor.
(3) The Clapeyron slope of phase transition at 660 km (C_{660}) plays significant roles in affecting the slab mode selection in the MTZ. Higher values of $|C660| > 2$ MPa/K can easily result in slab stagnation in the free subduction models, whereas lower values of $|C660| \leq 1$ MPa/K generally lead to slab penetration. The Clapeyron slope of 410 km (C_{410}) does not change the general mode of slab/MTZ interaction, which will however affect the trench motion and further the length of flattened slab.
(4) A sharp viscosity jump between the lower and upper mantles can promote slab stagnation in the MTZ, which has a similar effect with a strong viscosity-depth gradient, i.e. a gradually increasing viscosity with depth.
(5) The trench retreat is the most critical factor controlling slab stagnation, especially long slab flattening in the MTZ. The fast trench retreat with a constant velocity of ≥ 3 cm/yr will generally lead to long flattened slab in the MTZ. In contrast, the stable or slow retreating trench favors slab penetration into the lower mantle.
(6) The age/thickness of the subducting and overriding plates can also influence the slab/MTZ interaction, which generally takes effect by modifying the slab dip angle and trench motions.
(7) A thin, weak layer at the bottom of MTZ does not play crucial roles in the slab mode selection, which is thus contrasting to the global mantle convection model (Mao and Zhong, 2018) and may require further comparable studies.

Acknowledgments

This work was supported by the NSFC projects (grant numbers: 41622404, 41688103, 91855208, 41774108); the Strategic Priority Research Program (B) of Chinese Academy of Sciences (grant number: XDB18000000), as well as the support from the University of Chinese Academy of Sciences. Numerical simulations were run with the clusters of National Supercomputer Center in Guangzhou (Tianhe-II). N. Ribe, M. Gurnis and B. Steinberger are acknowledged for the helpful discussion. In addition, X. Zhou, Y.N. Shi and S.T. Yang are thanked for the assistance in compiling the observational datasets of natural subduction zones in Fig. 1 as well as the experimental datasets of Clapeyron slopes in Tables 1 and 2. Thorough and constructive reviews by the editor D. van Hinsbergen and two anonymous reviewers improved the paper. The authors declare no conflict of interest.

Appendix A. Supplementary data

Supplementary data to this article can be found online at https://doi.org/10.1016/j.earscirev.2019.05.018.

References

Agrusta, R., van Hunen, J., Goes, S., 2014. The effect of metastable pyroxene on the slab dynamics. Geophys. Res. Lett. 41, 8800–8808.

Agrusta, R., Goes, S., van Hunen, J., 2017. Subducting-slab transition zone interaction: stagnation, penetration and mode switches. Earth Planet. Sci. Lett. 464, 10–23.

Akaogi, M., Ito, E., 1993. Refinement of enthalpy measurement of $MgSiO_3$ perovskite and negative pressure-temperature slopes for perovskite-forming reactions. Geophys. Res. Lett. 20 (17), 1839–1842.

Akaogi, M., Ito, E., Navrotsky, A., 1989. Olivine-modified spinel-spinel transitions in the system Mg_2SiO_4-Fe_2SiO_4: calorimetric measurements, thermochemical calculation, and geophysical application. J. Geophys. Res. 94 (B11), 15671–15685.

Akaogi, M., Takayama, H., Kojitani, H., Kawaji, H., Atake, T., 2007. Low-temperature heat capacities, entropies and enthalpies of Mg_2SiO_4 polymorphs, and α-β-γ and post-spinel phase relations at high pressure. Phys. Chem. Miner. 34, 169–183.

Arredondo, K.M., Billen, M.I., 2016. The effects of phase transitions and compositional layering in two-dimensional kinematic models of subduction. J. Geodyn. 100, 159–174.

Ashida, T., Kume, S., Ito, E., 1987. Thermodynamic aspects of phase boundary among α-, β-, and γ-Mg_2SiO_4. In: Manghnani, M.H., Syono, Y. (Eds.), High-Pressure *Research in Mineral Physics*. AGU, Washington D.C., USA, pp. 269–274.

Auzanneau, E., Schmidt, M.W., Vielzeuf, D., Connolly, J.A.D., 2010. Titanium in phengite: a geobarometer for high temperature eclogites. Contrib. Mineral. Petrol. 159, 1–24.

Behn, M.D., Kelemen, P.B., 2003. Relationship between seismic P-wave velocity and the composition of anhydrous igneous and meta-igneous rocks. Geochem. Geophys. Geosyst. 4 (5), 1041.

Bellahsen, N., Faccenna, C., Funiciello, F., 2005. Dynamics of subduction and plate motion in laboratory experiments: insights into the "plate tectonics" behavior of the Earth. J. Geophys. Res. 110, B01401.

Billen, M.I., 2008. Modeling the dynamics of subducting slabs. Annu. Rev. Earth Planet. Sci. 36, 325–356.

Billen, M.I., 2010. Slab dynamics in the transition zone. Phys. Earth Planet. Inter. 183, 296–308.

Bina, C.R., Helffrich, G., 1994. Phase transition Clapeyron slopes and transition zone seismic discontinuity topography. J. Geophys. Res. 99 (B8), 15853–15860.

Bina, C.R., Stein, S., Marton, F.C., Van Ark, E.M., 2001. Implications of slab mineralogy for subduction dynamics. Phys. Earth Planet. Inter. 127, 51–66.

Bittner, D., Schmeling, H., 1995. Numerical modeling of melting processes and induced diapirism in the lower crust. Geophys. J. Int. 123, 59–70.

Capitanio, F.A., Morra, G., Goes, S., 2007. Dynamic models of downgoing plate-buoyancy driven subduction: subduction motions and energy dissipation. Earth Planet. Sci. Lett. 262, 284–297.

Capitanio, F.A., Stegman, D.R., Moresi, L.N., Sharples, W., 2010. Upper-plate controls on deep subduction, trench migration and deformation at convergent margins. Tectonophys 483, 80–92.

Chopelas, A., 1991. Thermal properties of β-Mg_2SiO_4 at mantle pressures derived from vibrational spectroscopy: implications for the mantle at 400 km depth. J. Geophys. Res. 96, 11817–11829.

Chopelas, A., Boehler, R., Ko, T., 1994. Thermodynamics and behavior of γ-Mg_2SiO_4 at High pressure: implications for Mg_2SiO_4 phase equilibrium. Phys. Chem. Miner. 21, 351–359.

Christensen, U.R., 1996. The influence of trench migration on slab penetration into the lower mantle. Earth Planet. Sci. Lett. 140 (1–4).

Christensen, U.R., Yuen, D.A., 1984. The interaction of a subducting lithosphere slab with a chemical or phase boundary. J. Geophys. Res. 89 (B6), 4389–4402.

Christensen, U.R., Yuen, D.A., 1985. Layered convection induced by phase transitions. J. Geophys. Res. 90 (B12), 4389–4402.

Čížková, H., Bina, C.R., 2013. Effects of mantle and subduction-interface rheologies on slab stagnation and trench rollback. Earth Planet. Sci. Lett. 379, 95–103.

Čížková, H., van Hunen, J., van der Berg, A., Vlaar, N.J., 2002. The influence of rheological weakening and yield stress on the interaction of slabs with the 670 km discontinuity. Earth Planet. Sci. Lett. 199, 447–457.

Čížková, H., van den Berg, A., Sparkman, W., Matyska, C., 2012. The viscosity of Earth's lower mantle inferred from sinking speed of subducted lithosphere. Phys. Earth Planet. Inter. 200-201, 56–62.

Clauser, C., Huenges, E., 1995. Thermal conductivity of rocks and minerals. In: Ahrens, T.J. (Ed.), Rock Physics and Phase Relations. American Geophysical Union, Reference Shelf 3, Washington D.C., pp. 105–126.

Coggon, R., Holland, T., 2002. Mixing properties of phengitic micas and revised garnet-phengite thermobarometers. J. Metamorph. Geol. 20, 683–696.

Connolly, J.A.D., 2005. Computation of phase equilibria by linear programming: a tool for geodynamic modeling and an application to subduction zone decarbonation. Earth Planet. Sci. Lett. 236, 524–541.

Connolly, J.A.D., 2009. The geodynamic equation of state: what and how. Geochem. Geophys. Geosyst. 10, Q10014.

Crameri, F., Lithgow-Bertelloni, C., 2018. Abrupt upper-plate tilting during slab-transition-zone collision. Tectonophys 746, 199–211.

Crameri, F., Schmeling, H., Golabek, G.J., Duretz, T., Orendt, R., Buiter, S., May, D., Kaus, B., Gerya, T.V., Tackley, P., 2012. A comparison of numerical surface topography calculations in geodynamic modelling: an evaluation of the 'sticky air' method. Geophys. J. Int. 189, 38–54.

DeMets, C., Gordon, R.G., Argus, D.F., Stein, S., 1994. Effect of recent revisions to the geomagnetic reversal time scale on estimates of current plate motions. Geophys. Res. Lett. 21, 2191–2194.

Di Giuseppe, E., van Hunen, J., Funiciello, F., Faccenna, C., Giardini, D., 2008. Slab stiffness control of trench motion: insights from numerical models. Geochem. Geophys. Geosyst. 9, Q02014.

Dziewonski, A.M., Anderson, D.L., 1981. Preliminary reference Earth model. *Phys. Earth* Planet. Inter. 25, 297–356.

Evans, B., Goetze, C., 1979. The temperature variation of hardness of olivine and its implication for polycrystalline yield stress. J. Geophys. Res. 84, 5505–5524.

Faccenda, M., Gerya, T., Mancktelow, N., Moresi, L., 2012. Fluid flow during slab unbending and dehydration: implications for intermediate-depth seismicity, slab weakening and deep water recycling. Geochem. Geophys. Geosyst. 13 (1), Q01010.

Fei, Y., Van Orman, J., Li, J., Van Westrenen, W., Sanloup, C., Minarik, W., Hirose, K., Komabayashi, T., Walter, M., Funakoshi, K., 2004. Experimentally determined postspinel transformation boundary in Mg_2SiO_4 using MgO as an internal pressure standard and its geophysical implications. J. Geophys. Res. 109, B02305.

Forte, A.M., Quéré, S., Moucha, R., Simmons, N.A., Grand, S.P., Mitrovica, J.X., Rowley, D.B., 2010. Joint seismic-geodynamic-mineral physical modelling of African geodynamics: a reconciliation of deep-mantle convection with surface geophysical constraints. Earth Planet. Sci. Lett. 295, 329–341.

Fuhrman, M.L., Lindsley, D.H., 1988. Ternary-Feldspar modeling and thermometry. Am. Mineral. 73, 201–215.

Fukao, Y., Obayashi, M., 2013. Subducted slabs stagnant above, penetrating through, and trapped below the 660 km discontinuity. J. Geophys. Res. 118, 5920–5938.

Funiciello, F., Faccenna, C., Heuret, A., Lallemand, S., Di Giuseppe, E., Becker, T.W., 2008. Trench migration, net rotation and slab-mantle coupling. Earth Planet. Sci. Lett. 271, 233–240.

Gale, A., Dalton, C.A., Langmuir, C.H., Su, Y., Schilling, J.G., 2013. The mean composition of ocean ridge basalts. Geochem. Geophys. Geosyst. 14 (3), 489–518.

Garel, F., Goes, S., Davies, D.R., Davies, J.H., Kramer, S.C., Wilson, C.R., 2014. Interaction of subducted slabs with the mantle transition zone: a regime diagram from 2-D thermo-mechanical models with a mobile trench and an overriding plate. Geochem. Geophys. Geosyst. 15, 1739–1765.

Gerya, T.V., 2010. Introduction to Numerical Geodynamic Modelling. Cambridge University Press, Cambridge, UK.

Gerya, T.V., Meilick, F.I., 2011. Geodynamic regimes of subduction under an active margin: effects of rheological weakening by fluids and melts. J. Metamorph. Geol. 29 (1), 7–31.

Gerya, T.V., Connolly, J.A.D., Yuen, D.A., Gorczyk, W., Capel, A.M., 2006. Seismic implications of mantle wedge plumes. Phys. Earth Planet. Inter. 156, 59–74.

Gerya, T.V., Perchuk, L.L., Burg, J.-P., 2008. Transient hot channels: perpetrating and regurgitating ultrahigh-pressure, high-temperature crust-mantle associations in collision belts. Lithos 103, 236–256.

Goes, S., Capitanio, F.A., Morra, G., 2008. Evidence for lower mantle slab penetration phases in plate motions. Nature 451, 981–984.

Goes, S., Capitanio, F.A., Morra, G., Seton, M., Giardini, D., 2011. Signatures of downgoing plate-buoyancy driven subduction in Cenozoic plate motions. Phys. Earth Planet. Inter. 184, 1–13.

Goes, S., Agrusta, R., van Hunen, J., Garel, F., 2017. Subduction-transition zone interaction: a review. Geosphere 13 (3), 644–664.

Gorczyk, W., Willner, A.P., Gerya, T., Connolly, J., Burg, J.-P., 2007. Physical controls of magmatic productivity at Pacific-type convergent margins: numerical modelling. Phys. Earth Planet. Inter. 163, 209–232.

Grand, S., van der Hilst, R.D., Widiyantoro, S., 1997. Global seismic tomography: a snapshot of convection in the Earth. GSA Today 7, 1–7.

Gurnis, M., Hager, B.H., 1988. Controls of the structure of subducted slabs. Nature 335, 317–321.

Hager, B.H., 1984. Subducted slabs and the geoid: constraints on mantle rheology and flow. J. Geophys. Res. 89 (B7), 6003–6015.

Hart, S.R., Zindler, A., 1986. In search of a bulk-Earth composition. Chem. Geo. 57, 247–267.

Hirose, K., 2002. Phase transitions in pyrolitic mantle around 670-km depth: implications for upwelling of plumes from the lower mantle. J. Geophys. Res. 107, 2078.

Hogrefe, A., Rubie, D.C., Sharp, T.G., Seifert, F., 1994. Metastability of enstatite in deep subducting lithosphere. Nature 372, 351–353.

Holland, T.J.B., Powell, R., 1996. Thermodynamics of order-disorder in minerals 2: symmetric formalism applied to solid solutions. Am. Mineral. 81, 1425–1437.

Holland, T.J.B., Powell, R., 1998. An internally consistent thermodynamic dataset for phases of petrological interest. J. Metamorph. Geol. 16, 309–343.

Holland, T.J.B., Baker, J., Powell, R., 1998. Mixing properties and activity-composition relationships of chlorites in the system MgO-FeO-Al_2O_3-SiO_2-H_2O. Eur. J. Mineral. 10, 395–406.

Holland, T.J.B., Hudson, N.F.C., Powell, R., Harte, B., 2013. New thermodynamic models and calculated phase equilibria in NCFMAS for basic and ultrabasic compositions through the transition zone into the uppermost lower mantle. J. Petrol. 54 (9), 1901–1920.

Holt, A.F., Becker, T.W., Buffett, B.A., 2015. Trench migration and overriding plate stress in dynamic subduction models. Geophys. J. Int. 201 (1), 172–192.

Huang, J., Zhao, D., 2006. High-resolution mantle tomography of China and surrounding

regions. J. Geophys. Res. 111, B09305.
Huangfu, P., Wang, Y., Cawood, P., Li, Z.-H., Fan, W., Gerya, T., 2016. Thermo-mechanical controls of flat subduction: insights from numerical modeling. Gondwana Res. 40, 170–183.
Ito, K., Kennedy, G., 1971. An experimental study of the basalt-garnet granulite-eclogite transition. In: Heacock, J.G. (Ed.), The Structure and Physical Properties of the Earth's Crust, Geophys. Monogr. Ser. vol. 14. AGU, Washington D.C., USA, pp. 303–314.
Ito, K., Kennedy, G., 2013. An experimental study of the basalt-garnet granulite-eclogite transition. In: Heacock, J.G. (Ed.), The Structure and Physical Properties of the Earth's Crust. American Geophysical Union, Washington, DC.
Ito, E., Takahashi, E., 1989. Postspinel transformations in the system Mg_2SiO_4–Fe_2SiO_4 and some geophysical implications. J. Geophys. Res. 94, 10637–10646.
Ito, E., Yamada, H., 1982. Stability relations of silicate spinels, ilmenites and perovskites. In: Akimoto, S., Maghnani, M.H. (Eds.), High-Pressure Research in Geophysics. Springer, The Netherlands, pp. 405–419.
Ito, E., Akaogi, M., Topor, L., Navrotsky, A., 1990. Negative pressure-temperature slopes for reactions forming MgSiO3 perovskite from calorimetry. Science 249, 1275–1278.
Kameyama, M., Yuen, D.A., Karato, S.-I., 1999. Thermal-mechanical effects of low-temperature plasticity (the peierls mechanism) on the deformation of viscoelastic shear zone. Earth Planet. Sci. Lett. (1–2), 159–172.
Karato, S.I., 2008. Deformation of Earth Materials: An Introduction to the Rheology of Solid Earth. Cambridge University Press, Cambridge, UK.
Karato, S.I., 2011. Water distribution across the mantle transition zone and its implications for global material circulation. Earth Planet. Sci. Lett. 301, 413–423.
Karato, S., Wu, P., 1993. Rheology of the upper mantle: a synthesis. Science 260 (5109), 771–778.
Karato, S., Riedel, M., Yuen, D.A., 2001. Rheological structure and deformation of subducted slabs in the mantle transition zone: implications for mantle circulation and deep earthquakes. Phys. Earth Planet. Inter. 127, 83–108.
Katayama, I., Karato, S.I., 2008. Low-temperature, high-stress deformation of olivine under water-saturated conditions. Phys. Earth Planet. Inter. 168, 125–133.
Katsura, T., Ito, E., 1989. The system Mg_2SiO_4-Fe_2SiO_4 at high pressures and temperatures: precise determination of stabilities of olivine, modified spinel, and spinel. J. Geophys. Res. 94 (B11), 15663–15670.
Katsura, T., Yamada, H., Shinmei, T., Kubo, A., Ono, S., Kanzaki, M., Yoneda, A., Walter, M., Ito, E., Urakawa, S., Funakoshi, K., Utsumi, W., 2003. Post-spinel transition in Mg2SiO4 determined by high P-T in situ X-ray diffractometry. Phys. Earth Planet. Inter. 136, 11–24.
Katz, R.F., Spiegelman, M., Langmuir, C.H., 2003. A new parameterisation of hydrous mantle melting. Geochem. Geophys. Geosyst. 4, 1073.
King, S.D., 2001. Subduction zones: observations and geodynamic models. Phys. Earth Planet. Inter. 127, 9–24.
King, S.D., Frost, D.J., Rubie, D.C., 2015. Why cold slabs stagnate in the transition zone. Geology 43, 231–234.
Kirby, S.H., Kronenberg, A.K., 1987. Rheology of the lithosphere: selected topics. Rev. Geophys. 25, 1219–1244.
Kocks, U.F., Argon, A.S., Ashby, M.F., 1975. Thermodynamics and kinetics of slip. Prog. Mater. Sci. 19, 1–281.
Lallemand, S., Heuret, A., Boutelier, D., 2005. On the relationships between slab dip, backarc stress, upper plate absolute motion, and crustal nature in subduction zones. Geochem. Geophys. Geosyst. 6, Q09006.
Li, Z.-H., 2014. A review on the numerical geodynamic modeling of continental subduction, collision and exhumation. Sci. China Earth Sci. 57, 47–69.
Li, Z.-H., Ribe, N.M., 2012. Dynamics of free subduction from 3-D boundary element modeling. J. Geophys. Res. Solid Earth 117, B06408.
Li, Z.H., Gerya, T., Burg, J.P., 2010. Influence of tectonic overpressure on P-T paths of HP-UHP rocks in continental collision zones: thermomechanical modeling. J. Metamorph. Geol. 28, 227–247.
Li, Z.-H., Di Leo, J.F., Ribe, N.M., 2014. Subduction-induced mantle flow, finite strain and seismic anisotropy: numerical modeling. J. Geophys. Res. Solid Earth 119 (6), 5052–5076.
Li, Z.-H., Liu, M.Q., Gerya, T., 2015. Material transportation and fluid-melt activity in the subduction channel: numerical modeling. Sci. China Earth Sci. 58, 1251–1268.
Li, Z.-H., Liu, M., Gerya, T., 2016. Lithosphere delamination in continental collisional orogens: a systematic numerical study. J. Geophys. Res. Solid Earth 121, 5186–5211.
Litasov, K., Ohtani, E., Sano, A., Suzuki, A., 2005a. Wet subduction versus cold subduction. Geophys. Res. Lett. 32, L13312.
Litasov, K., Ohtani, E., Sano, A., Suzuki, A., Funakoshi, K., 2005b. In situ X-ray diffraction study of post-spinel transformation in a peridotite mantle: implication for the 660-km discontinuity. Earth Planet. Sci. Lett. 238, 311–328.
Liu, M.-Q., Li, Z.-H., Yang, S.-H., 2017. Diapir versus along-channel ascent of crustal material during plate convergence: constrained by the thermal structure of subduction zones. J. Asian Earth Sci. 145, 16–36.
Mao, W., Zhong, S., 2018. Slab stagnation due to a reduced viscosity layer beneath the mantle transition zone. Nat. Geo. 11, 876–881.
Mitrovica, J.X., Forte, A.M., 2004. A new inference of mantle viscosity based upon joint inversion of convection and glacial isostatic adjustment data. Earth Planet. Sci. Lett. 225, 177–189.
Morishima, H., Kato, T., Suto, M., Ohtani, E., Urakawa, S., Utsumi, W., Shimomura, O., Kikegawa, T., 1994. The phase boundary between α- and β-Mg_2SiO_4 determined by in Situ X-ray observation. Science 265, 1202–1203.
Mosenfelder, J.L., Marton, F.C., Ross, C.R., Kerschhofer, L., Rubie, D.C., 2001. Experimental constraints on the depth of olivine metastability in subducting lithosphere. Phys. Earth Planet. Inter. 127, 165–180.
Müller, R.D., Sdrolias, M., Gaina, C., Roest, W.R., 2008. Age, spreading rates and spreading asymmetry of the world's ocean crust. Geochem. Geophys. Geosyst. 9, Q04006.
Nishi, M., Kato, T., Kubo, T., Kikegawa, T., 2008. Survival of pyropic garnet in subducting plates. Phys. Earth Planet. Inter. 170, 264–280.
Obayashi, M., Yoshimitsu, J., Nolet, G., Fukao, Y., Shiobara, H., Sugioka, H., Miyamachi, H., Gao, Y., 2013. Finite frequency whole mantle P wave tomography: improvement of subducted slab images. Geophys. Res. Lett. 40, 5652–5657.
O'Neill, C., Müller, D., Steinberger, B., 2005. On the uncertainties in hot spot reconstructions and the significance of moving hot spot reference frames. Geochem. Geophys. Geosyst. 6, Q04003.
Padrón-Navarta, J., Sánchez-Vizcaíno, V., Hermann, J., Connolly, J.A.D., Garrido, C.J., Gómez-Pugnaire, M.T., Marchesi, C., 2013. Tschermak's substitution in antigorite and consequences for phase relations and water liberation in high-grade serpentinites. Lithos 178, 186–196.
Peacock, S.M., 1990. Fluid processes in subduction zones. Science 248, 329–337.
Plank, T., Langmuir, C.H., 1998. The chemical composition of subducting sediment and its consequences for the crust and mantle. Chem. Geo. 145, 325–394.
Quinquis, M., Buiter, S., 2014. Testing the effects of basic numerical implementations of water migration on models of subduction dynamics. Solid Earth 5, 537–555.
Ranalli, G., 1995. Rheology of the Earth, Deformation and Flow Process in Geophysics and Geodynamics, 2nd ed. Chapman & Hall, London, UK.
Ringwood, A.E., 1975. Composition and Petrology of the Earth's Mantle. McGraw-Hill, New York, USA.
Rodríguez-González, J., Negredo, A.M., Billen, M.I., 2012. The role of the overriding plate thermal state on slab dip variability and on the occurrence of flat subduction. Geochem. Geophys. Geosyst. 13, Q01002.
Rubie, D.C., Ross, C.R., 1994. Kinetics of the olivine-spinel transformation in subducting lithosphere: experimental constraints, and implications for deep slab processes. Phys. Earth Planet. Inter. 86, 223–241.
Schellart, W.P., 2008. Overriding plate shortening and extension above subduction zones: a parametric study to explain formation of the Andes mountains. Geol. Soc. Am. Bull. 120, 1441–1454.
Schellart, W.P., Stegman, D.R., Freeman, J., 2008. Global trench migration velocities and slab migration induced upper mantle volume fluxes: constraints to find an Earth reference frame based on minimizing viscous dissipation. Earth-Sci. Rev. 88, 118–144.
Schellart, W.P., Stegman, D.R., Farrington, R.J., Moresi, L., 2011. Influence of lateral slab edge distance on plate velocity, trench velocity, and subduction partitioning. J. Geophys. Res. 116, B10408.
Schmeling, H., Babeyko, A.Y., Ennsa, A., Faccenna, C., Funiciello, F., Gerya, T., Golabek, G.J., Grigull, S., Kaus, B., Morra, G., Schmalholz, S., Van Hunen, J., 2008. A benchmark comparison of spontaneous subduction models-Towards a free surface. Phys. Earth Planet. Inter. 171, 198–223.
Schmidt, M.W., Poli, S., 1998. Experimentally based water budgets for dehydrating slabs and consequences for arc magma generation. Earth Planet. Sci. Lett. 163, 361–379.
Sdrolias, M., Müller, R.D., 2006. Controls on back-arc basin formation. Geochem. Geophys. Geosyst. 7, Q04016.
Shi, Y., Wei, D., Li, Z.-H., Liu, M.-Q., Liu, M., 2018. Subduction Mode selection during slab and mantle transition zone interaction: numerical modeling. Pure Appl. Geophys. 175, 529–548.
Sizova, E., Gerya, T., Stüwe, K., Brown, M., 2015. Generation of felsic crust in the Archean: a geodynamic modeling perspective. Precambrian Res. 271, 198–224.
Steinberger, B., 2007. Effects of latent heat release at phase boundaries on flow in the Earth's mantle, phase boundary topography and dynamic topography at the Earth's surface. Phys. Earth Planet. Inter. 164, 2–20.
Steinberger, B., Calderwood, A.R., 2006. Models of large-scale viscous flow in the Earth's mantle with constraints from mineral physics and surface observations. Geophys. J. Int. 167, 1461–1481.
Stixrude, L., Lithgow-Bertelloni, C., 2011. Thermodynamics of mantle minerals-II phase equilibria. Geophys. J. Int. 184, 1180–1213.
Suito, K., 1977. Phase relations of pure Mg_2SiO_4 up to 200 kilobars. In: Manghnani, M.H., Akimoto, S. (Eds.), High-Pressure Research - Applications in Geophysics. Academic, San Diego, USA, pp. 255–266.
Tackley, P.J., Stevenson, D.J., Glatzmaier, G.A., Schubert, S., 1993. Effects of an endothermic phase transition at 670 km depth in a spherical model of convection in the Earth's mantle. Nature 361, 699–704.
Tetzlaff, M., Schmeling, H., 2009. Time-dependent interaction between subduction dynamics and phase transition kinetics. Geophys. J. Int. 178, 826–844.
Turcotte, D.L., Schubert, G., 2002. Geodynamics. Cambridge University Press, Cambridge, UK.
Van der Hilst, R.D., 1995. Complex morphology of subducted lithosphere in the mantle beneath the Tonga trench. Nature 374, 154–157.
Van der Hilst, R.D., Seno, T., 1993. Effects of relative plate motion on the deep structure and penetration depth of slabs below the Izu-Bonin and Mariana island arcs. Earth Planet. Sci. Lett. 120, 395–407.
Van Mierlo, W.L., Langenhorst, F., Frost, D.J., Rubie, D.C., 2013. Stagnation of subducting slabs in the transition zone due to slow diffusion in majoritic garnet. Nat. Geo. 6, 400–403.
Wei, C.J., Powell, R., 2003. Phase relations in high-pressure metapelites in the system KFMASH (K_2O-FeO-MgO-Al_2O_3-SiO_2-H_2O) with application to natural rocks. Contrib. Mineral. Petrol. 145, 301–315.
White, R.W., Powell, R., Phillips, G.N., 2003. A mineral equilibria study of the hydrothermal alteration in mafic greenschist facies rocks at Kalgoorlie, Western Australia. J. Metamorph. Geol. 21, 455–468.

Williams, S., Flament, N., Müller, R.D., Butterworth, N.P., 2015. Absolute plate motions since 130 Ma constrained by subduction zone kinematics. Earth Planet. Sci. Lett. 418, 66–77.
Yanagisawa, T., Yamagishi, Y., Hamano, Y., Stegman, D.R., 2010. Mechanism for generating stagnant slabs in 3-D spherical mantle convection models at Earth-like conditions. Phys. Earth Planet. Inter. 183, 341–352.
Yang, J., Zhao, L., Kaus, B., Lu, G., Wang, K., Zhu, R., 2018a. Slab-triggered wet upwellings produce large volumes of melt: insights into the destruction of the North China Craton. Tectonophys 746, 266–279.
Yang, T., Moresi, L., Zhao, D., Sandiford, D., Whittaker, J., 2018b. Cenozoic lithospheric deformation in Northeast Asia and the rapidly-aging Pacific Plate. Earth Planet. Sci. Lett. 492, 1–11.
Yang, S.-H., Li, Z.-H., Gerya, T., Xu, Z.-Q., Shi, Y.-L., 2018c. Dynamics of terrane accretion during seaward continental drifting and oceanic subduction: numerical modeling and implications for the Jurassic crustal growth of the Lhasa Terrane, Tibet. Tectonophys 746, 212–228.
Zahirovic, S., Müller, R.D., Seton, M., Flament, N., 2015. Tectonic speed limits from plate kinematic reconstructions. Earth Planet. Sci. Lett. 418, 40–52.
Zhong, S., Gurnis, M., 1994. Role of plates and temperature-dependent viscosity in phase change dynamics. J. Geophys. Res. 99, 15903–15917.